1   **Carbon Monitoring System Flux Net Biosphere Exchange 2020 (CMS-Flux NBE 2020)**

3   Junjie Liu[1,2*], Latha Baskaran[1], Kevin Bowman[1], David Schimel[1], A. Anthony Bloom[1], Nicholas
4   C. Parazoo[1], Tomohiro Oda[3,4], Dustin Carroll[5], Dimitris Menemenlis[1], Joanna Joiner[3], Roisin
5   Commane[6], Bruce Daube[7], Lucianna V. Gatti[8], Kathryn McKain[9,10], John Miller[9], Britton B.
6   Stephens[11], Colm Sweeney[9], Steven Wofsy[7],
7
8
9   1. Jet Propulsion Laboratory, Caltech, CA
10   2. Caltech, CA
11   3. Global Modeling and Assimilation Office, NASA Goddard Space Flight Center,
12   Greenbelt, MD
13   4. Goddard Earth Sciences Technology and Research, Universities Space Research
14   Association, Columbia, MD
15   5. Moss Landing Marine Laboratories, San José State University, California, CA
16   6. Lamont-Doherty Earth Observatory of Columbia University, NY
17   7. Harvard University, Cambridge, MA
18   8. LaGEE, CCST, INPE- National Institute for Space Researc, Brazil
19   9. NOAA, Global Monitoring Laboratory, Boulder, CO 80305
20   10. University of Colorado, Cooperative Institute for Research in Environmental Sciences,
21   Boulder, CO
22   11. National Center for Atmospheric Research, Boulder, CO 80301
23   Correspondence: Junjie Liu (junjie.liu@jpl.nasa.gov)

26   **Abstract**. Here we present a global and regionally-resolved terrestrial net biosphere exchange
27   (NBE) dataset with corresponding uncertainties between 2010–2018: CMS-Flux NBE 2020. It is
28   estimated using the NASA Carbon Monitoring System Flux (CMS-Flux) top-down flux
29   inversion system that assimilates column CO_2 observations from Greenhouse gases Observing
30   SATellite (GOSAT) and the NASA's Observing Carbon Observatory -2 (OCO-2). The regional
31   monthly fluxes are readily accessible as tabular files, and the gridded fluxes are available in
32   NetCDF format. The fluxes and their uncertainty estimates are evaluated by extensively
33   comparing the posterior CO_2 mole fractions with aircraft CO_2 observations. We describe the
34   characteristics of the dataset as global total, regional climatological mean, and regional annual
35   fluxes and seasonal cycles. We find that the global total fluxes of the dataset agree with
36   atmospheric CO_2 growth observed by the surface-observation network within uncertainty.
37   Averaged between 2010 and 2018, the tropical regions range from close-to neutral in tropical
38   South America to a net source in Africa; these contrast with the extra-tropics, which are a net
39   sink of 2.5 ± 0.3 gigaton carbon per year. The regional satellite-constrained NBE estimates
40   provide a unique perspective for understanding the terrestrial biosphere carbon dynamics and
41   monitoring changes in regional contributions to the changes of atmospheric CO_2 growth rate.
42   The gridded and regional aggregated dataset can be accessed at:
43   https://doi.org/10.25966/4v02-c391 (Liu et al., 2020).

1 Introduction

47 New "top-down" inversion frameworks that harness satellite observations provide an important

48 complement to global aggregated fluxes (e.g., Global Carbon Project, Friedlingstein et al., 2019)

49 and inversions based on surface CO_2 observations (e.g., Crowell et al., 2019). These satellite-

50 constrained estimates resolve regional fluxes, and also disentangle net biosphere exchange (NBE)

51 into constituent carbon fluxes including plant gross primary productivity (GPP) and biomass

52 burning through solar-induced fluorescence and carbon monoxide proxies, respectively (Bowman

53 et al, 2017, Liu et al., 2017). Both the spatial and process resolution are critical for evaluating

54 models and reducing uncertainties about future carbon-climate feedbacks (e.g., Friedlingstein et

55 al., 2014). The NBE are far more variable than ocean fluxes (Lovenduski and Bonan, 2017) or

56 fossil fuel emissions (Yin et al, 2019), and are thus the focus of this dataset estimated from a top-

57 down atmospheric CO_2 inversion of satellite column CO_2 dry-air mole fraction (X_{CO2}). We present

58 the global and regional NBE dataset as a series of maps, time series and tables, and disseminate it

59 as a public dataset for further analysis and comparison to other sources of flux information. Finally,

60 we provide a comprehensive evaluation of both mean and uncertainty estimates against an

61 independent airborne dataset. Subsequent papers will present the partitioning of the NBE into

62 constituent gross fluxes.

63

64 Global top-down atmospheric CO_2 flux inversions have been historically used to estimate regional

65 terrestrial NBE, which is a sum of net ecosystem exchange and biomass burning carbon fluxes.

66 They make uses of the spatiotemporal variability of atmospheric CO_2, which is dominated by NBE,

67 to infer net carbon exchange at the surface (Chevallier et al., 2005; Baker et al., 2006; Liu et al.,

68 2014). The accuracy of the NBE from top-down flux inversion is determined by the density and

69   accuracy of the CO_2 observations, the accuracy of modeled atmospheric transport, and knowledge

70   of the prior uncertainties of the flux inventories.

71

72   For CO_2 flux inversions based on high precision *in situ* and flask observations, the measurement

73   error is low (<0.2 parts per million (ppm)) and not a significant source of error; however, these

74   observations are limited spatially, and are concentrating primarily over North America (NA) and

75   Europe (Crowell et al., 2019). Satellite X_{CO2} from CO_2-dedicated satellites, such as the Greenhouse

76   Gases Observing Satellite (GOSAT) (launched in July 2009) and the Observing Carbon

77   Observatory 2 (OCO-2) (Crisp et al., 2017) have much broader spatial coverage (O'Dell et al.,

78   2018), and fill the observational gaps of conventional surface CO_2 observations, but they have up

79   to an order of magnitude higher single-sounding uncertainty and potential systematic errors

80   compared to the *in situ* and flask CO_2 observations. Recent progress in instrument error

81   characterization, spectroscopy, and retrieval methods have significantly improved the accuracy

82   and precision of the X_{CO2} retrievals (O'Dell et al., 2018; Kiel et al., 2019). The single sounding

83   random error of X_{CO2} from OCO-2 is ~1.0 ppm (Kulawik et al., 2019). A recent study by Byrne et

84   al. (2020) shows less than a 0.5 ppm difference between posterior X_{CO2} constrained by a recent

85   data set, ACOS-GOSAT b7 X_{CO2} retrievals, and those constrained by conventional surface CO_2

86   observations. Chevallier et al. (2019) also showed that OCO-2 based flux inversion had similar

87   performance to surface CO_2 based flux inversions when comparing posterior CO_2 mole fractions

88   to aircraft CO_2 in the free troposphere. Results from these studies show that systematic

89   uncertainties in CO_2 retrievals from satellites are comparable to, or smaller than, other uncertainty

90   sources in atmospheric inversions (e.g. transport).

91

92   A newly-developed biogeochemical model-data fusion system, CARDAMOM, made progress in

93   producing NBE uncertainties, along with mean values that are consistent with a variety of

94   observations assimilated through a Markov Chain Monte Carlo (MCMC) method (Bloom et al.,

95   2016; 2020). Transport model errors in general have also been reduced relative to earlier transport

96   model intercomparison efforts, such as TRANSCOM 3 (Gurney et al., 2004; Gaubert et al., 2019).

97   Advancements in satellite retrieval, transport, and prior terrestrial biosphere modeling have led to

98   more mature inversions constrained by satellite X_{CO2} observations.

99

100   Two satellites, GOSAT and OCO-2, have now produced more than 10 years of observations. Here

101   we harness the CMS-Flux inversion framework (Liu et al., 2014; 2017; 2018; Bowman et al., 2017)

102   to generate an NBE product: CMS-Flux NBE 2020, by assimilating both GOSAT and OCO-2 from

103   2010–2018. The dataset is the longest satellite-constrained NBE product so far. The CMS-Flux

104   framework exploits globally available X_{CO2} to infer spatially-resolved total surface-atmosphere

105   exchange, which can be subsequently decomposed into individual fluxes using ancillary

106   measurements (i.e., GPP, respiration, fires, fossil fuel, etc.). The flux estimates from the CMS-

107   Flux framework have been used to assess the impacts of El Niño on terrestrial biosphere fluxes

108   (Bowman et al, 2017; Liu et al, 2017) and the role of droughts in the North America (NA) carbon

109   balance (Liu et al, 2018). These fluxes have furthermore been ingested into land-surface data

110   assimilation systems to quantify heterotrophic respiration (Konings et al., 2019), evaluate

111   structural and parametric uncertainty in carbon-climate models (Quetin et al., 2020), and inform

112   climate dynamics (Bloom et al., 2020). We present the regional NBE and its uncertainty based on

113   two types of regional masks: (1) latitude and continent; and)2) distribution of biome types (defined

114   by plant functional types), and continent. The gridded NBE dataset and its uncertainty are also

115   available, so that users can aggregate the fluxes and uncertainties based on self-defined regions.

116

117   The outline of the paper is as follows: Section 2 describes methods, and Sections 3 and 4 describe

118   the dataset and the major NBE characteristics, respectively. We extensively evaluate the posterior

119   fluxes and uncertainties by comparing the posterior CO_2 mole fractions against aircraft

120   observations and a gross primary production (GPP) product (section 5). In Section 6, we discuss

121   the strength and weakness, and potential usage of the data. A summary is provided in Section 7,

122   and Section 8 is dataset availability and future plan.

123

124   **2   Methods**

125   **2.1 CMS-Flux inversion system**

126   The CMS-Flux framework is summarized in Figure 1. The center of the system is the CMS-Flux

127   inversion system, which optimizes NBE and air-sea net carbon exchanges with a 4D-Var inversion

128   system (Liu et al., 2014). In the current system, we assume that no uncertainty in fossil fuel

129   emissions, since the uncertainty in fossil fuel emissions at regional scales is substantially less than

130   NBE uncertainties, which is a widely adopted assumption in global flux inversion systems (e.g.,

131   Crowell et al., 2019). The 4D-Var minimizes a cost function that include the sum of two terms:

132    $$J(\mathbf{x}) = (\mathbf{x} - \mathbf{x}_b)^T \mathbf{B}^{-1}(\mathbf{x} - \mathbf{x}^b) + (\mathbf{y} - h(\mathbf{x}))^T \mathbf{R}^{-1}(\mathbf{y} - h(\mathbf{x})) \quad (1)$$

133   The first term measures the differences between the optimized fluxes and the prior fluxes

134   normalized by the prior flux error covariance **B**, and the second term measures the differences

135   between observations ($\mathbf{y}$) and the corresponding model simulated value ($h(\mathbf{x})$) normalized by the

136   observation error covariance **R**. The term $h(\cdot)$ is the observation operator that calculates

137   observation-equivalent model-simulated X_{CO2}. The 4D-Var uses the adjoint (i.e., the backward

138   integration of the transport model) (Henze et al., 2004) of the GEOS-Chem transport model to

139   calculate the sensitivity of the observations to surface fluxes. The configurations of the inversion

140   system are summarized in Table 1. We run both the forward and adjoint at 4° x 5° spatial resolution,

141   and optimize monthly NBE and air-sea carbon fluxes at each grid point from January 2010 to

142   December 2018. Inputs for the system include prior carbon fluxes, meteorological drivers, and the

143   satellite X_{CO2} (Figure 1). Section 2.2 (Table 2) describes the prior flux and its uncertainties, and

144   section 2.3 (Table 3) describes the observations and the corresponding uncertainties.

145

146   **2.2 The prior CO₂ fluxes and uncertainties**

147   Prior CO₂ fluxes include NBE, air-sea net carbon fluxes, and fossil fuel emissions (see Table 2).

148   The data sources for the prior fluxes are listed in Table 7. Methods to generate prior ocean carbon

149   fluxes and fossil fuel emissions are documented in Brix et al., (2015), Caroll et al. (2020), and Oda

150   et al. (2018). The focus of this dataset is optimized terrestrial biosphere fluxes, so we briefly

151   describe the prior terrestrial biosphere fluxes and its uncertainties.

152

153   We construct the NBE prior using the CARDAMOM framework (Bloom et al., 2016).

154   CARDAMOM data assimilation system explicitly represents the time-resolved uncertainties in

155   NBE. The prior estimates are already constrained with multiple data streams accounting for

156   measurement uncertainties following a similar Bayesian approach used in the 4D-variational

157   approach. We use the CARDAMOM setup as described by Bloom et al. (2016, 2020) resolved at

158   monthly timescales; data constraints include GOME-2 solar-induced fluorescence (Joiner et al.,

159   2013), MODIS Leaf Area Index (LAI), and biomass and soil carbon (details on the data

160   assimilation are provided in Bloom et al. (2020)). In addition, mean GPP and fire carbon emissions

161   from2010 - 2017 are constrained by FLUXCOM GPP (Tramontana et al., 2016) and GFEDv4.1s

162   (Randerson et al., 2018) respectively, both assimilated with an uncertainty of 20%. We use the

163   Olsen and Randerson (2001) approach to downscale monthly GPP and respiration fluxes to 3-

164   hourly timescales, based on ERA-interim re-analysis of global radiation and surface temperature.

165   Fire fluxes are downscaled using the GFEDv4.1 daily and diurnal scale factors on monthly

166   emissions (Giglio et al., 2013). Posterior CARDAMOM NBE estimates are then summarized as

167   NBE mean and standard deviation values.

168

169   The NBE from CARDAMON shows net carbon uptake of 2.3 GtC/year over the tropics and close

170   to neutral in the extratropics (Figure S1). The year-to-year variability (i.e., interannual variability,

171   IAV) estimated from CARDAMOM from 2010 –2017 is generally less than 0.1 $gC/m^2/day$ outside

172   of the tropics (Figure S1). Because of the weak interannual variability estimated by CARDAMOM,

173   we use the same 2017 NBE prior for 2018.

174

175   CARDAMOM generates uncertainty along with the mean state. The relative uncertainty over the

176   tropics is generally larger than 100%, and the magnitude is between 50% and 100% over the extra-

177   tropics (Figure S2). We assume no correlation in prior flux errors in either space or time. Temporal

178   and spatial error correlation estimates can in principle be computed by CARDAMOM. We

179   anticipate incorporating these error correlations in subsequent versions of this dataset.

180

181   **2.3 Column CO_2 observations from GOSAT and OCO-2**

182   We use satellite-column CO_2 retrievals from Atmospheric Carbon Observations from Space

183   (ACOS) team for both GOSAT (version 7.3) and OCO-2 (version 9) (Table 3). The use of the

184   same retrieval algorithm and validation strategy adopted by ACOS team to process both GOSAT

185   and OCO-2 spectra maximize the consistency between these two datasets. Both GOSAT and OCO-

186   2 satellites carry high-resolution spectrometers optimized to return high precision measurements

187   of reflected sunlight within CO_2 and O_2 absorption bands in the shortwave infrared (Crisp et al.,

188   2012). Both satellites fly in a sun-synchronous orbit. GOSAT has a 13:00 ± 0.15 hours local

189   crossing time and a three-day ground track repeat cycle. The footprint of GOSAT is ~10.5 km in

190   diameter in sun-nadir view (Crisp et al., 2012). The daily number of soundings processed by the

191   ACOS-GOSAT retrieval algorithm is between a few hundreds to ~2000. Further quality control

192   and filtering reduce the ACOS-GOSAT X_{CO2} retrievals to 100 – 300 daily (Figure S5 in Liu et al.,

193   2017). We only assimilate ACOS-GOSAT land nadir good quality observations.

194

195   OCO-2 has a 13:30 local crossing time and 16-day ground track repeat cycle. The nominal

196   footprints of OCO-2 are 1.25 km wide and ~2.4 km along the orbit. Because of its small footprint

197   and sampling strategy, OCO-2 has many more X_{CO2} retrievals than ACOS-GOSAT. OCO-2 has

198   four observing modes: land nadir, land glint, ocean glint, and target. Following Liu et al. (2017),

199   we only use land nadir observations from OCO-2 to generate a set of super observations by

200   aggregating the observations within ~100 km (along the same orbit). The super observations have

201   more uniform spatial coverage and are more comparable to the spatial representation of ACOS-

202   GOSAT observations (see Figure S5 in Liu et al., 2017).

203

204   We directly use observational uncertainty provided with ACOS-GOSAT b7.3 to represent the

205   observation error, **R**, in Eq 1. The uncertainty of the OCO-2 super observations is the sum of the

206   variability of X_{CO2} used to generate each individual super observation and the mean uncertainty

207   provided in the original OCO-2 retrievals. More detailed information about OCO-2 super

208   observations can be found in Liu et al. (2017). Kulawik et al. (2019) showed that both OCO-2 and

209   ACOS-GOSAT bias-corrected retrievals have mean biases of -0.1 ppm when compared against

210   X_{CO2} from Total Carbon Column Observing Network (TCCON) (Wunch et al., 2011), indicating

211   consistency between ACOS-GOSAT and OCO-2 retrievals. The magnitude of observation errors

212   used in **R** is generally above 1.0 ppm, larger than the sum of random error and biases in the

213   observations. The ACOS-GOSAT b7.3 observations from July 2009–June 2015 are used to

214   optimize fluxes between 2010 and 2014, and the OCO-2 X_{CO2} observations from Sep 2014–June

215   2019 are used to optimize fluxes between 2015 and 2018.

216

217   The observational coverage of ACOS-GOSAT and OCO-2 is spatiotemporally dependent, with

218   more coverage during summer than winter over the NH, and more observations over mid-latitudes

219   than over the tropics (Figure S3). The variability (i.e., standard deviation) of annual total number

220   of observations from 2010–2014 is within 4% of the annual mean number for ACOS-GOSAT.

221   Except for a data gap in 2017 caused by a malfunction of OCO-2 instrument, the variability of

222   annual total number of observations between 2015 and 2018 is within 8% of the annual mean

223   number for OCO-2.

224

225   **2.4 Uncertainty quantification**

226   The posterior flux error covariance is analytically the inverse Hessian, which incorporates the

227   transport, measurement, and background errors at the 4D-Var solution (Eq. 13 in Bowman et al,

228   2017). For large-order systems, the posterior errors cannot be explicitly calculated. Consequently,

229   we rely on a Monte Carlo approach to quantify posterior flux uncertainties following Chevallier et

230   al. (2010) and Liu et al. (2014). In this approach, an ensemble of flux inversions is carried out with

231 an ensemble of priors and simulated observations to sample the uncertainties of prior fluxes (i.e.,

232 **B** in eq. 1) and observations (**R** in Eq. 1), respectively. The magnitude of posterior flux

233 uncertainties is a function of assumed uncertainties in prior fluxes and observations, as well as the

234 density of observations. Since the density of GOSAT and OCO-2 observations are stable (section

235 2.3) within their respective data record, we characterize the posterior flux uncertainties for 2010

236 and 2015 only, and assume the flux uncertainties for 2011–2014 are the same as 2010 and flux

237 uncertainties for 2016–2018 are the same as 2015.

238 **2.5 Evaluation of posterior fluxes**

239 Direct NBE estimates from flux towers only provide a spatial representation of a few kilometers

240 (Running et al., 1999), not appropriate to evaluate regional NBE from top-down flux inversions.

241 Thus, we use two methods to indirectly evaluate the posterior NBE and its uncertainties. One is to

242 compare annual NBE anomalies and seasonal cycle to a gross primary production (GPP) product.

243 The other is to compare posterior CO_2 mole fractions to independent aircraft observations (i.e., not

244 assimilated in the inversion). The second method has been broadly used to indirectly evaluate

245 posterior fluxes from top-down flux inversions (e.g., Stephens et al., 2007; Liu and Bowman, 2016;

246 Chevallier et al., 2019; Crowell et al., 2019).

247 **2.5.1 Evaluation against independent gross primary production (GPP) product**

248   NBE is a small residual difference between two large terms: total ecosystem respiration (TER)

249 and GPP, plus fire. A positive NBE anomaly (i.e., less uptake from the atmosphere) has been

250 shown to correspond to reduced GPP caused by climate anomalies (e.g., Bastos et al., 2018), and

251 the magnitude of net uptake is proportional to GPP in most biomes observed by flux tower

252 observations (e.g, Falk et al., 2008). Since NBE is related not only to GPP, the comparison to GPP

253 only serves as a qualitative measure of the NBE quality. For example, we would expect that the

254   posterior NBE seasonality to be anti-correlated with GPP in the temperate and high latitudes. In

255   this study, we use FLUXSAT GPP (Joiner et al., 2018), which is an upscaled GPP product based

256   on flux tower GPP observations and satellite-based geometry adjusted reflectance from the

257   MODerate-resolution Imaging Spectroradiometer (MODIS) and solar-induced chlorophyll

258   fluorescence observations from Global Ozone Monitoring Experiment – 2 (GOME-2) (Joiner et

259   al., 2013). Joiner et al. (2018) show that the agreement between FLUXSAT-GPP and GPP from

260   flux towers is better than other available upscaled GPP products.

261   **2.5.2 Evaluation against aircraft CO_2 observations**

262   The aircraft observations used in this study include those published in ObsPack August 2019

263   (CarbonTracker team, 2019), which include regular vertical profiles from flask samples collected

264   on light aircraft by NOAA (Sweeney et al., 2015) and other laboratories, aircraft campaigns from

265   Atmospheric Tomography (ATom, Wofsy et al., 2018) and HIAPER Pole-to-Pole (HIPPO, Wofsy

266   et al., 2011), regular (two to four weekly) vertical profiles from the Instituto de Pesquisas Espaciais

267   (INPE) over tropical South America (SA) (Gatti et al., 2014), and the O_2/N_2 Ratio and CO_2

268   airborne Southern Ocean (ORCAS) Study aircraft campaign (Stephens et al., 2017) (Table 3).

269   Figure 2 shows the aircraft observation coverage and density between 2010 and 2018. Most of the

270   aircraft observations are concentrated over NA. ATom had four (1–4) campaigns between August

271   2016 to May 2018, spanning four seasons over the Pacific and Atlantic Ocean. HIPPO had five

272   (1–5) campaigns over Pacific, and only HIPPO 3–5 occurred between 2010 and 2011. HIPPO 1–

273   2 occurred in 2009. Based on the spatial distribution of aircraft observations, we divide the

274   comparison into nine regions: Alaska, mid-latitude NA, Europe, East Asia, South Asia, Africa,

275   Australia, Southern Ocean, and South America (Table 4 and Figure 2).

276

277   We calculate several quantities to evaluate the posterior fluxes and its uncertainty with aircraft

278   observations. One is the monthly mean differences between posterior and aircraft CO_2 mole

279   fractions. The second is the monthly root mean square errors (RMSE) over each nine sub-regions,

280   which is defined as:

281     $$RMSE = \left(\frac{1}{n}\sum_{i=1}^{n}(y^o_{aircraft} - y^b_{aircraft})^2_i\right)^{\frac{1}{2}} \quad (2)$$

282   where $y^o_{aircraft}$ is i^{th} aircraft observation, $y^b_{aircraft}$ is the corresponding posterior CO_2 mole

283   fractions sampled at i^{th} aircraft locations, and n is the number of aircraft observations over each

284   region. The RMSE is computed over the n aircraft observations within one of the nine sub-regions.

285   The mean differences indicate the magnitude of mean posterior CO_2 bias, while the RMSE

286   includes both random and systematic errors in posterior CO_2. The bias and RMSE could be due to

287   errors in either posterior fluxes or transport or both. When transport errors are smaller than errors

288   in posterior fluxes, the magnitude of biases and *RMSE* indicates the accuracy of posterior fluxes.

289

290   To evaluate the magnitude of posterior flux uncertainty estimates, we compare *RMSE* against the

291   standard deviation of ensemble simulated aircraft observations (equation 3) from the Monte Carlo

292   method ($RMSE_{MC}$). The quantity $RMSE_{MC}$ can be written as:

293     $$RMSE_{MC} = \left[\frac{1}{nens}\sum_{iens=1}^{nens}\left((y^{b(MC)}_{aircraft})_{iens} - \bar{y}^{b(MC)}_{aircraft}\right)^2\right]^{\frac{1}{2}} (3)$$

294   The variable $(y^{b(MC)}_{aircraft})_{iens}$ is the ith ensemble member of simulated aircraft observations from

295   Monte Carlo ensemble simulations, $\bar{y}^{b(MC)}_{aircraft}$ is the mean, and *nens* is the total number of ensemble

296   members. For simplicity, in equation (3), we drop the indices for the aircraft observations used in

297   equation (2). In the absence of transport errors, when the estimated posterior flux uncertainty

298   reflects the "*true*" posterior flux uncertainty, we show in the *Appendix* that:

299    $RMSE^2 = R_{aircraft} + RMSE_{MC}{}^2$ (4)

300   where $R_{aircraft}$ is the aircraft observation error variance, which could be neglected on regional

301   scales. We further calculate the ratio r between $RMSE$ and $RMSE_{MC}$:

302    $r = \frac{RMSE}{RMSE_{MC}}$ (5)

303   A ratio close to one indicates that the posterior flux uncertainty reflects the true uncertainty in the

304   posterior fluxes when the transport errors are small.

305

306   The presence of transport errors will make the comparison between $RMSE$ and $RMSE_{MC}$

307   potentially difficult to interpret. Even when $RMSE_{MC}$ represents the actual uncertainty in posterior

308   fluxes, the $RMSE$ could be larger than $RMSE_{MC}$, since the differences between aircraft

309   observations and model simulated posterior mole fractions $RMSE$ could be due to errors in both

310   transport and the posterior fluxes, while $RMSE_{MC}$ only reflects the impact of posterior flux

311   uncertainty on simulated aircraft observations. In this study, we assume the primary sources of

312    $RMSE$ come from errors in posterior fluxes.

313

314   The $RMSE$ and $RMSE_{MC}$ comparison only shows differences in CO_2 space. We further calculate

315   the sensitivity of $RMSE$ to posterior flux using GEOS-Chem adjoint. We first define a cost

316   function J as:

317    $J = RMSE^2$ (6)

318   The sensitivity of the mean-square error to a flux, x, at location i and month j is

319    $w_{i,j} = \frac{\partial J}{\partial x_{i,j}} \times x_{i,j}$ (7)

320   This sensitivity is normalized by the flux magnitude. Equation 7 can be interpreted as the

321   sensitivity of the $RMSE^2$ to a fractional change in the fluxes. We can estimate the time-integrated

322   magnitude of the sensitivity over the entire assimilation window by calculating:

323     $S_i = \dfrac{\sum_{j=1}^{M}|w_{i,j}|}{\sum_{k=1}^{P}\sum_{j=1}^{M}|w_{k,j}|}$ (8)

324   where P is the total number of grid points and M is the total number of months from the time of

325   the aircraft data to the beginning of the inversion. The numerator of equation (8) quantifies the

326   absolute total sensitivity of the $RMSE^2$ to the fluxes at the ith grid. Normalized by the total absolute

327   sensitivity across the globe, the quantity S_i indicates the relative sensitivity of $RMSE^2$ to fluxes at

328   the ith grid point. Note that S_i is unitless, and it only quantifies sensitivity, not the contribution of

329   fluxes at each grid to $RMSE^2$.

330

2.6 Regional masks

331

332   We provide posterior NBE from 2010 – 2018 using two sets of aggregated regions, for a few

333   selected FLUXNET tower sites, and the underlying gridded product. The regional mask in Figure

334   3A is based on a combination of seven plant function types condensed from MODIS IGBP and the

335   TRANSCOM -3 region mask (Gurney et al., 2004). There are 28 regions in Figure 3A: six in NA,

336   four in SA, five in Eurasia (north of 40˚N), three in tropical Asia, three in Australia, and seven in

337   Africa. The regional mask in Figure 3B is based on latitude and continents, and there are 13 regions

338   in total.

339

3 Dataset description

340

341

342   We present the gridded fluxes as globally, latitudinally, and regionally time series. We show the

343   nine-year average fluxes aggregated into 28 and 13 geographic regions (Figure 3). The

344   aggregations are geographic (latitude and continent), bio-climatic (biome by continent), and flux-

345   oriented (for a set of selected flux sites). For each region in the geographic and biome aggregations,

346   we show nine-year mean annual net fluxes and uncertainties, and then the annual fluxes for each

347   region as a set of time-series plots. The month-by-month fluxes and uncertainties are available in

348   tabular format, so the actual aggregated fluxes may be readily compared to bottom-up extrapolated

349   fluxes and Earth System models. Users can also aggregate the gridded fluxes and uncertainties

350   based on their own defined regional masks. Table 5 provides a complete list of all data products

351   available in the dataset. In section 4, we describe the major characteristics of the dataset.

352   **4 Characteristics of the dataset**

353   **4.1 Global fluxes**

354   The annual atmospheric CO_2 growth rate, which is the sum of fossil fuel emissions and total annual

355   sink over land and ocean, is well-observed by NOAA surface CO_2 observing network

356   (https://www.esrl.noaa.gov/gmd/ccgg/ggrn.php) (Freidlingstein et al., 2019). We compare the global total

357   flux estimates constrained by GOSAT and OCO-2 with the NOAA CO_2 growth rate from 2010–

358   2018, and discuss the mean carbon sink over land and ocean. Over these nine years, the satellite-

359   constrained atmospheric CO_2 growth rate agrees with the NOAA observed CO_2 growth rate within

360   the uncertainty of posterior fluxes (Figure 4). The mean annual global surface CO_2 flux (in Gt C/yr)

361   is derived from the NOAA observed CO_2 growth rate (in ppm/yr) using a conversion factor of

362   2.124 GtC/ppm (Le Quéré et al., 2018). The estimated growth rate has the largest discrepancy with

363   the NOAA observed growth rate in 2014, which may be due to a failure of one of the two solar

364   paddles in May 2014 (Kuze et al., 2016). Over the nine years, the estimated total accumulated

365   carbon in the atmosphere is 41.5 ± 2.4 GtC, which is slightly lower than the accumulated carbon

366   based on NOAA CO_2 growth rate (45.2 ± 0.4 GtC). On average, the land sink is $20 \pm 8\%$ of fossil

367 fuel emissions, and the ocean sink is 30 ± 1% of fossil fuel emissions (Figure 4). These numbers

368 are within the ranges of the corresponding estimates from GCP 2019 (Freidlingstein et al., 2019).

369 The mean NBE and ocean sink from GCP 2019 are 21 ± 10% (~1.0 GtC estimated residual NBE

370 uncertainty) and 26 ± 5% (~0.5 GtC estimated ocean flux uncertainty) of fossil fuel emissions

371 respectively between 2010–2018. The GCP NBE here is calculate as the residual differences

372 between fossil fuel, ocean fluxes, and atmospheric CO_2 growth rate, and it is also equivalent to the

373 sum of carbon fluxes from land use changes, land sink, and residual balance reported by GCP.

374 Over these nine years, we estimate that the land sink ranges from 37% of fossil fuel emissions in

375 2011 (a La Niña year) to only 5% in 2015 (an El Niño year), consistent with GCP estimated range

376 of 35% in 2011 to 7% in 2015. We estimate that the ocean sinks range from 39% in 2015 to 23%

377 of fossil fuel emissions in 2012, larger than the GCP estimated ocean flux ranges of 25% to 28%

378 of fossil fuel emissions (Freidlingstein et al., 2019).

379 **4.2 Mean regional fluxes and uncertainties**

380 Figure 5 shows the nine-year mean regional annual fluxes, uncertainty, and its variability between

381 2010–2018. Table 6 shows an example of the dataset corresponding to Figure 5 A, C, and E. It

382 shows large net carbon uptake occurs over Eurasia, NA, and Southern Hemisphere (SH) mid-

383 latitudes. The largest net carbon uptake is over eastern US (-0.4 ± 0.1 GtC (1σ uncertainty)) and

384 high latitude Eurasia (-0.4 ± 0.1 GtC) (Figure 5A, B). We estimate a net land carbon sink of 2.5 ±

385 0.3 GtC/year between 2010–2013 over the NH mid to high latitudes, which agrees with 2.4 ± 0.6

386 GtC estimates over the same time periods based on a two-box model (Ciais et al., 2019). Net uptake

387 in the tropics ranges from close-to-neutral in tropical South America (0.0 ± 0.1 GtC) to a net source

388 in northern Africa (0.6 ± 0.2 GtC) (Figure 5A, B). The tropics exhibit both large uncertainty and

389 large variability. The NBE interannual variability over northern Africa and tropical SA are 0.5 GtC

390   and 0.3 GtC respectively, larger than the 0.2 GtC and 0.1 GtC uncertainty (Figure 5C, D). We also

391   find collocation of regions with large NBE and GPP interannual variability (Figure S4).

392

393   **4.3 Interannual variabilities and uncertainties**

394   Here we present hemispheric and regional NBE interannual variabilities and corresponding

395   uncertainties (Figures 6 and 7, and corresponding tabular data files). In Figure 6, we further divide

396   the globe into three large latitude bands: tropics (20°S–20°N), NH extra-tropics (20°N–85°N), and

397   SH extra-tropics (60°S–20°S). The tropical NBE contributes 90% to the global NBE interannual

398   variability (IAV). The IAV of NBE over the extra-tropics is only about one-third of that over the

399   tropics. The dominant role of tropical NBE in the global IAV of NBE agrees with Figure 4 in

400   Sellers et al. (2018). The top-down global annual NBE anomaly is within the 1.0 GtC/yr

401   uncertainty of residual NBE (i.e., fossil fuel – atmospheric growth – ocean sink) calculated from

402   GCP-2019 (Friedlinston et al., 2019) (Figure 6).

403

404   Figure 7 shows the annual NBE anomalies and uncertainties over a few selected regions. Positive

405   NBE indicates reduced net uptake relative to the 2010–2018 mean, and vice versa. Also shown in

406   Figure 7 are GPP anomalies estimated from FLUXSAT. Positive GPP indicates increased

407   productivity, and vice versa. GPP drives NBE in years where anomalies are inversely correlated

408   (e.g., positive NBE and negative GPP), and TER drives NBE in years where anomalies of GPP

409   and NBE have the same sign or weakly correlated. Over tropical SA evergreen broadleaf forest,

410   the largest positive NBE anomalies occur during 2015–2016 El Niño, corresponding to large

411   reductions in productively, consistent with Liu et al. (2017). In 2017, the region sees increased net

412   uptake and increased productivity, implying a recovery from the 2015–2016 El Niño event. The

413   variability in GPP explains 80% of NBE variability over this region over the nine-year period. In

414   Australian shrubland, our inversion captures the increased net uptake in 2010 and 2011 due to

415   increased precipitation (Pouter et al., 2014) and increased productivity. The variability in GPP

416   explains 70% of the interannual variability in NBE. Over tropical south America Savanna, the

417   NBE interannual variability also shows strong negative correlations with GPP, with GPP

418   explaining 40% of NBE interannual variability. Over the mid-latitude regions where the IAV is

419   small, the R^2 between GPP and NBE is also small (0.0–0.5) as expected. But the increased net

420   uptake generally corresponds to increased productivity. We also do not expect perfect negative

421   correlation between NBE anomalies and GPP anomalies, as discussed in section 2.5. The

422   comparison between NBE and GPP provides insight into when and where net fluxes are likely

423   dominated by productivity.

424

425   **4.4 Seasonal cycle**

426   We provide a top-down CO_2 constrained regional mean NBE seasonal cycle and its variability and

427   uncertainty. The seasonal cycle of NBE, including its phase (i.e., transition from source to sink)

428   and amplitude (peak-to-trough difference), have large uncertainties, not only over the less-

429   observed tropical regions, but also over the extra-tropics (e.g., Yang et al., 2007; Keppel-Aleks et

430   al., 2012). Figure 8 shows NBE and GPP seasonal cycles for six selected regions. In general, the

431   months that have larger productivity corresponds to months with a net uptake of carbon from the

432   atmosphere. The NH mid-to-high latitudes have larger seasonal cycle amplitudes (Figure 8A, B)

433   compared to the other regions, and their NBE seasonalities are more closely linked to that of GPP

434   ($R^2 = 0.9$). In the tropics, the relationship between NBE and GPP seasonality is less clear partially

435   due to the weak seasonality of NBE (Figure 8E, F). The variability and uncertainty of monthly

436   mean fluxes are larger over the tropics and the SH extratropics than over the NH extratropics.

437   **5   Evaluation against independent aircraft CO_2 observations**

438   **5.1 Comparison to aircraft observations over nine sub-regions**

439   In this section, we evaluate posterior CO_2 against aircraft observations over nine sub-regions listed

440   in Table 4 and Figure 2. We compare the posterior to aircraft CO_2 mole fractions above planetary

441   boundary layer and up to mid troposphere (1–5 km) at the locations and time of aircraft

442   observations, and then calculate the monthly mean error statistics between 1–5 km. The aircraft

443   observations between 1–5 km are more sensitive to regional fluxes (Liu et al., 2015; Liu and

444   Bowman, 2016). Scatter plots in the left column of Figure 9 show regional monthly mean de-

445   trended aircraft CO_2 observations (x-axis) versus the simulated detrended posterior CO_2 (y-axis).

446   We used NOAA global CO_2 trend to detrend both the observations and model simulated mole

447   fractions (ftp://aftp.cmdl.noaa.gov/products/trends/co2/co2_trend_gl.txt). Over the NH regions (A,

448   B, C, D) and Africa (F), the R^2 is equal or above 0.9, which indicates that the posterior CO_2 captures

449   the observed seasonality. The low R^2 (0.7) value in South Asia is caused by one outlier. Over

450   Southern Ocean, Australia, and SA, the R^2 is between 0.2 and 0.4, reflecting weaker CO_2

451   seasonality over these regions.

452

453   The right panel of Figure 9 shows the monthly mean differences between posterior CO_2 and aircraft

454   observations (black), the number of aircraft observations (blue bar, right y-axis), *RMSE* (equation

455   2) (blue line), and *RMSE$_{MC}$* (equation 3) (red line). The magnitude of mean differences between

456   posterior CO_2 and aircraft observations is less than 0.5 ppm except over Southern Ocean, which

457   has a -0.8 ppm bias. The mean differences between posterior CO_2 and aircraft observations are

458 primarily caused by errors in transport and biases in assimilated satellite observations, while

459 $RMSE_{MC}$ is 'internal flux error' projected into mole fraction space.   With the exception of the

460 Southern Ocean, for all regions mean bias is significantly less than $RMSE_{MC}$, which suggests that

461 transport and data bias in satellite observations may be much smaller than the internal flux errors.

462

463 As demonstrated in section 2.5, comparing $RMSE$ and $RMSE_{MC}$ is a test of the accuracy of posterior

464 flux uncertainty estimate. Over all the regions, the differences between $RMSE$ and $RMSE_{MC}$ are

465 smaller than 0.3 ppm, which indicates a comparable magnitude between empirical posterior flux

466 uncertainty estimates from Monte Carlo method and the actual posterior flux uncertainty over the

467 regions that these aircraft observations are sensitive to. These aircraft observations are sensitive to

468 fluxes over a broad region as shown in Figure S5.

469

470 **5.2 Comparison to aircraft observations from ATom and HIPPO aircraft campaigns**

471 Figures 10 and 11 show comparisons to aircraft CO_2 from ATom 1–4 campaigns spanning four

472 seasons, and HIPPO 3–5 over the Pacific Ocean between 1–5 km. The vertical curtain comparisons

473 are shown in Figure S6 and S7. The mean differences between posterior CO_2 and aircraft CO_2 are

474 quite uniform (within 0.5 ppm) throughout the column except over the Atlantic Ocean during

475 ATom 1–2 and the Southern Ocean during ATom 1 (Figures S6 and S7). Also shown in Figures

476 10 and 11 are $RMSE$ of each aircraft campaign (middle column) and the ratio between $RMSE$ and

477 $RMSE_{MC}$ (right column). A ratio larger than one between $RMSE$ and $RMSE_{MC}$ indicates errors in

478 either transport or low of posterior flux uncertainty estimates (section 2.5).

479

480   Over most of flight tracks during ATom 1–4, the posterior CO_2 errors are between -0.5 and 0.5

481   ppm, the *RMSE* is smaller than 0.5 ppm, and the ratio between *RMSE* and $RMSE_{MC}$ is smaller than

482   or equal to 1. However, off the coast of Africa during ATOM -1 and -2 and over Southern Ocean

483   during ATOM-1, the mean differences between posterior CO_2 and aircraft observations are larger

484   than 0.5 ppm. During ATOM-1 (29 July – 23 Aug 2016), the mean differences between posterior

485   CO_2 and aircraft CO_2 show large negative biases, while during ATOM-2 (26 Jan 2017–21 Feb

486   2017), it has large positive biases off the coast of Africa. The ratio between *RMSE* and $RMSE_{MC}$

487   is significantly larger than one over these regions, which indicates an underestimation of posterior

488   flux uncertainty or large magnitude of transport errors during that time period.

489

490   We further run adjoint sensitivity analyses over the three regions with ratios significantly larger

491   than one to identify the posterior fluxes that could contribute to the large differences between

492   posterior CO_2 and aircraft observations during ATOM 1–2. We run the adjoint model backward

493   for three months from the observation time and calculate S_i defined in equation (7). Adjoint

494   sensitivity analysis indicates that the large mismatch between aircraft observations and model

495   simulations during ATOM-1 and -2 off the coast of Africa could be potentially driven by errors in

496   posterior fluxes over tropical Africa (Figure S8). These large posterior CO_2 errors and large ratio

497   over Southern Ocean during ATOM-1 are driven by flux errors in oceanic fluxes around 30°S and

498   over Australia (Figure S9).

499

500   During the HIPPO aircraft campaigns, the absolute errors in posterior CO_2 across Pacific are less

501   than 0.5 ppm except over the Arctic Ocean and over Alaska in summer (Figure 11), consistent

502   with Figure 10A. The large errors over the Arctic Ocean may be related to both transport errors

503   and the accuracy of high latitude fluxes. Byrne et al. (2020) provide a brief summary of these

504   challenges in simulating CO_2 over high latitudes with 4° x 5° resolution transport model.

505   Increasing the resolution of the transport model may reduce transport errors over high latitudes.

506

507   We run adjoint sensitivity analysis over the high-latitude regions where the differences between

508   posterior CO_2 and aircraft observations are large (Figure 11). The adjoint sensitivity analysis

509   (Figure S10) shows that the large errors over these regions could be driven by errors in fluxes over

510   Alaska as well as broad NH mid-latitude regions.

511
512   **6   Discussion**

513   Evaluation of posterior flux uncertainty estimates by comparing posterior CO_2 error statistics

514   (*RMSE,* Equation 2) with the standard deviation of ensemble simulated CO_2 from Monte Carlo

515   uncertainty quantification method (*$RMSE_{MC}$*, equation 3) has its limitations. When *RMSE* and

516   *$RMSE_{MC}$* are similar in magnitude, this indicates small magnitude of transport errors and

517   reasonable posterior uncertainty estimates. A much larger *RMSE* than *$RMSE_{MC}$* could be due to

518   errors in either transport or underestimation of posterior flux uncertainty or both. The presence of

519   transport errors makes the interpretation of the *RMSE* and *$RMSE_{MC}$* complex. A better, independent

520   quantification of transport errors is needed in the future in order to rigorously use the comparison

521   statistics between aircraft observations and posterior CO_2 to diagnose flux errors.

522

523   Comparison to aircraft observations shows regionally-dependent accuracy in posterior fluxes.

524   ATom observations show seasonally-dependent biases over the Atlantic, implying possible

525   seasonally dependent errors in posterior fluxes over northern to central Africa. Therefore, we

526   recommend combining NBE with other ancillary variables, e.g., GPP, to better understand carbon

527   dynamics. Combining NBE with component carbon fluxes can shed light on the processes

528   controlling the changes of NBE (e.g., Bowman et al, 2017; Liu et al., 2017). NBE can be written

529   as:

530   NBE= TER + fire - GPP   (8)

531   where TER is total ecosystem respiration (TER) (Figure 1). Satellite carbon monoxide (CO)

532   observations provide constraints on fire emissions (Arellano et al, 2006, van der Werf, 2008; Jones

533   et al, 2009; Jiang et al., 2015, Bowman et al, 2017; Liu et al., 2017). In addition to FLUXSAT-

534   GPP product used here, solar induced chlorophyll fluorescence (SIF) can be directly used as a

535   proxy for GPP (e.g., Parazoo et al, 2014). Once NBE, fire, and GPP carbon fluxes are quantified,

536   TER can be calculated as a residual (e.g., Bowman et al, 2017; Liu et al., 2017, 2018).

537

538   Because of the diffusive manner of atmospheric transport and the limited observation coverage,

539   the gridded flux values are not independent from each other. The errors and relative uncertainties

540   of the fluxes at each individual grid point are larger than regional aggregated fluxes. For the same

541   reason, comparing NBE with flux tower observations needs caution, though we provide NBE at a

542   few flux tower sites.

543

544   The variability and changes are more robust than the mean NBE fluxes from top-down flux

545   inversions in general (Baker et al., 2006b). The errors in transport and potential biases in

546   observations are mostly stable in time, so biases in the mean fluxes tend to cancel out when

547   computing interannual variability and year-to-year changes (Schuh et al., 2019; Crowell et al.,

548   2019).

549

550 The global fossil fuel emissions have ~5% uncertainty (GCP, 2019). However, they are regionally

551 inhomogeneous. We neglect the uncertainties in fossil fuel emissions, which will introduce

552 additional error in regions of rapid fossil fuel growth or in areas with noisier statistics (Yin et al.,

553 2019). In the future, we will account for uncertainties in fossil fuel emissions.

554

555 The posterior NBE includes all types of land fluxes except fossil fuel emissions, which is

556 equivalent to the sum of land use change fluxes and land sinks published by GCP. The sum of

557 regional NBE and fossil fuel emissions is an index of the contribution of any specific region to the

558 changes of atmospheric CO_2 growth rate. Even over the continental US, where fossil fuel

559 emissions are ~1.5 GtC/year, the changes of regional NBE can significantly modify contributions

560 to the changes of atmospheric CO_2 (Liu et al., 2018). Since NBE has high variability and its

561 predicted changes in the future are likely to have large uncertainties, quantifying regional NBE is

562 critical to monitoring regional contributions to atmospheric CO_2 growth rate, and ultimately to

563 guide mitigation to limit warming to 1.5°C above pre-industrial level (IPCC, AR6).

564

565 **7   Summary**

566 Terrestrial biosphere carbon fluxes are the largest contributor to the interannual variability of the

567 atmospheric CO_2 growth rate. Therefore, monitoring its change at regional scales is essential for

568 understanding how it responds to CO_2, climate and land use. Here, we present the longest terrestrial

569 flux estimates and their uncertainties constrained by X_{CO2} from 2010–2018 on self-consistent

570 global and regional scales (CMS-Flux NBE 2020). We qualitatively evaluate the net flux estimates

571 by comparing its variability with GPP variability, and provide comprehensive evaluation of

572 posterior fluxes and the uncertainties by comparing posterior CO_2 with independent aircraft CO_2.

573   The estimated posterior flux uncertainty agrees with the expected uncertainty in the posterior

574   fluxes based on the comparison to aircraft CO_2 observations. This dataset can be used in

575   understanding controls on regional NBE interannual variability, evaluating biogeochemical

576   models, and provide support the monitoring of the regional contributions to the changes in

577   atmospheric CO_2.

578

579   **8   Data availability and future update**

580   The CMS-Flux NBE 2020 data is available at: https://doi.org/10.25966/4v02-c391 (Liu et al.,

581   2020). The regional aggregated fluxes are provided as *csv* files with file size ~10MB, and the

582   gridded data is provided in NetCDF format with file size ~10MB. The full ensemble posterior

583   fluxes used to estimate posterior flux uncertainties are provided in NetCDF format with file size

584   ~20MB. Table 7 lists the sources of the data used in producing and evaluating the CMS-Flux NBE

585   2020 data product.

586

587   The quality of X_{CO2} from satellite observations is continually improving. The OCO-2 v10 X_{CO2}

588   will be released in June 2020, and the full GOSAT record (June 2009–Jan 2020) processed by the

589   same retrieval algorithm as OCO-2 will be released around the same time. Continuing to improving

590   the quality of satellite observations and extending the NBE estimates beyond 2018 in the future

591   will help us better understand interactions between terrestrial biosphere carbon cycle and climate

592   and provide support in monitoring the regional contributions to the changes of atmospheric CO_2.

593   Thus, we plan a future update of the dataset on an annual basis, with a goal to support current

594   scientific research and policy making.

595   **9   Author contributions**

596 JL designed the study and led the writing of the paper in close collaboration with KB and DS. LB

597 helped generate the plots and created all the data files. AAB provided the prior of the terrestrial

598 biosphere carbon fluxes. NP helped interpret the GPP evaluation. DM and DC generated the prior

599 ocean carbon fluxes. TO generated the ODIAC fossil fuel emissions. JJ provided the FLUXSAT

600 GPP product. BD and SW provided and contributed to the interpretation of HIPPO aircraft CO_2

601 observation comparisons. BS, KM, and CS provided ORCAS aircraft CO_2 observations and

602 contributed interpretation of aircraft CO_2 observation comparisons. LVG and JM provided INPE

603 aircraft CO_2 observations and contributed interpretation of aircraft CO_2 observation comparisons.

604 CS and KM provided ATom and NOAA aircraft CO2 observations and contributed interpretation

605 of aircraft CO_2 observation comparisons. We furthermore acknowledge funding from the EU for

606 the ERC project "ASICA" (grant number 649087) to Wouter Peters (Groningen University) and

607 EU and NERC (UK) funding to Emanuel Gloor (University of Leeds), which contributed to the

608 INPE Amazon greenhouse sampling program. All authors contributed to the writing, and have

609 reviewed and approved the paper.

610 **10 Competing interest**

611 The authors declare that they have no conflict of interest.

612 **Acknowledgement**

613 Resources supporting this work were provided by the NASA High-End Computing (HEC)

614 Program through the NASA Advanced Supercomputing (NAS) division at Ames Research Center.

615 We acknowledge the funding support from NASA OCO-2/3 Science Team, Carbon Monitoring

616 System (CMS), and Making Earth Science Data Records for Use in Research Environments

617 (MEaSUREs) programs. Tomohiro Oda is supported by the NASA Carbon Cycle Science program

618 (grant no. NNX14AM76G). We acknowledge EU and NERC (UK) funding to Emanuel

619   Gloor, University of Leeds which substantially contributed to the INPE Amazon

620   greenhouse sampling program. Part of the research was carried out at Jet Propulsion

621   Laboratory, Caltech.

622

623   **Appendix**

624   As shown in Kalnay (2003):

625    $RMSE^2 = R_{aircraft} + HP^aH^T$ (A.1)

626   where $R_{aircraft}$ is the aircraft observation error variance, and P^a is the posterior flux error

627   covariance. The H is linearized observation operator, which transfers posterior flux errors to

628   aircraft observation space, and H^T is its adjoint. In the Monte Carlo method, the postieror flux

629   error covariance P^a is approximated by:

630    $P^a = \frac{1}{nens} X^a X^{aT}$ (A.2)

631   where X^a is the ensemble perturbations written as:

632    $X^a = x^a - \bar{x}^a$ (A.3)

633   where x^a is the ensemble posterior fluxes from Monte Carlo, and $\bar{x}^a$ is the mean.

634   Therefore, HP^aH^T can be written as:

635    $HP^aH^T = \frac{1}{nens}[h(x^a) - h(\bar{x}^a)][h(x^a) - h(\bar{x}^a)]^T$ (A.4)

636   The right hand side is the same as the definiation of $RMSE_{MC}$ in the main text.

637   Therefore, when the posterior flux uncertainty estimated by Monte Carlo method represents the

638   actual uncertainty in posterior fluxes, equation (A.1) can be written as:

639    $RMSE^2 = R_{aircraft} + RMSE_{MC}^2$ (A.5).

640   It is the same as equation (3) in the main text.

641   References

642   Arellano Jr, A.F., Kasibhatla, P.S., Giglio, L., Van der Werf, G.R., Randerson, J.T., and Collatz,
643   G.J.: Time-dependent inversion estimates of global biomass-burning CO emissions using
644   Measurement of Pollution in the Troposphere (MOPITT) measurements, J. Geophys. Res:
645   Atmos., 111, D09303, https://doi.org/10.1029/2005JD006613, 2006.

646

647   Baker, D.F., Doney, S.C., and Schimel, D.S.: Variational data assimilation for atmospheric
648   CO2, Tellus B: Chem. Phys. Meteorol., 58, 359-365, https://doi.org/10.1111/j.1600-
649   0889.2006.00218.x, 2006a.

650

651   Baker, D.F., Law, R.M., Gurney, K.R., Rayner, P., Peylin, P., Denning, A.S., Bousquet, P.,
652   Bruhwiler, L., Chen, Y.H., Ciais, P., and Fung, I.Y.: TransCom 3 inversion intercomparison:
653   Impact of transport model errors on the interannual variability of regional CO2 fluxes, 1988–
654   2003, Global Biogeochem. Cy., 20, GB1002, https://doi.org/10.1029/2004GB002439, 2006b.

655

656   Bastos, A., Friedlingstein, P., Sitch, S., Chen, C., Mialon, A., Wigneron, J.-P., Arora, V.
657   K., Briggs, P. R., Canadell, J. G., and Ciais, P.: Impact of the 2015/2016 El Niño on the terrestrial
658   carbon cycle constrained by bottom-up and top-down approaches. Philos. Trans. R Soc. Lond. B.
659   Biol. Sci., 373, 1760, https://doi.org/10.1098/rstb.2017.0304, 2018.

660

661   Bloom, A.A., Exbrayat, J.F., van der Velde, I.R., Feng, L., and Williams, M.: The decadal state of
662   the terrestrial carbon cycle: Global retrievals of terrestrial carbon allocation, pools, and residence
663   times. Proc. Natl Acad. Sci., 113, 1285-1290, 2016.

664

665   Bloom, A. A., Bowman, K. W., Liu, J., Konings, A. G., Worden, J. R., Parazoo, N. C., Meyer, V.,
666   Reager, J. T., Worden, H. M., Jiang, Z., Quetin, G. R., Smallman, T. L., Exbrayat, J.-F., Yin, Y.,
667   Saatchi, S. S., Williams, M., and Schimel, D. S.: Lagged effects dominate the inter-annual
668   variability of the 2010–2015 tropical carbon balance, Biogeosciences Discuss.,
669   https://doi.org/10.5194/bg-2019-459, in review, 2020.

670

671   Bowman, K.W., Liu, J., Bloom, A.A., Parazoo, N.C., Lee, M., Jiang, Z., Menemenlis, D., Gierach,
672   M.M., Collatz, G.J., Gurney, K.R., and Wunch, D.: Global and Brazilian carbon response to El
673   Niño Modoki 2011–2010, Earth Space Sci., 4, 637-660, https://doi.org/10.1002/2016EA000204,
674   2017.

675

676   Brix, H., Menemenlis, D., Hill, C., Dutkiewicz, S., Jahn, O., Wang, D., Bowman, K., and Zhang,
677   H.: Using Green's Functions to initialize and adjust a global, eddying ocean biogeochemistry
678   general circulation model, Ocean Model., 95, 1-14, https://doi.org/10.1016/j.ocemod.2015.07.008,
679   2015.

680

681   Byrd, R.H., Nocedal, J., and Schnabel, R.B.: Representations of quasi-Newton matrices and their
682   use in limited memory methods, Math. Program., 63, 129-156,
683   https://doi.org/10.1007/BF01582063, 1994.

684

685 Byrne, B., Liu, J., et al.: Improved constraints on northern extratropical CO2 fluxes obtained by
686 combining surface-based and space-based atmospheric CO2 measurements, *JGR-Atmosphere*,
687 (*minor revision*), 2020

689 Carroll, D., Menemenlis, D., Adkins, J.: The ECCO-Darwin Data-assimilative Global Ocean
690 Biogeochemistry Model: Estimates of Seasonal to Multi-decadal Surface Ocean pCO2 and Air-
691 sea CO2 Flux. *Journal of Advances in Modeling Earth Systems* (*minor revision*), 2020

693 Chevallier, F., Fisher, M., Peylin, P., Serrar, S., Bousquet, P., Bréon, F.M., Chédin, A., and Ciais,
694 P.: Inferring CO2 sources and sinks from satellite observations: Method and application to TOVS
695 data, J. Geophys. Res.-Atmos., 110, D24309, https://doi.org/10.1029/2005JD006390, 2005.

697 Chevallier, F., Ciais, P., Conway, T.J., Aalto, T., Anderson, B.E., Bousquet, P., Brunke, E.G.,
698 Ciattaglia, L., Esaki, Y., Fröhlich, M., and Gomez, A.: CO_2 surface fluxes at grid point scale
699 estimated from a global 21 year reanalysis of atmospheric measurements, J. Geophys. Res., 115,
700 D21307, https://doi.org/10.1029/2010JD013887, 2010.

702 Chevallier, F., Remaud, M., O'Dell, C. W., Baker, D., Peylin, P., and Cozic, A.: Objective
703 evaluation of surface- and satellite-driven carbon dioxide atmospheric inversions, Atmos. Chem.
704 Phys., 19, 14233–14251, https://doi.org/10.5194/acp-19-14233-2019, 2019.

706 Ciais, P., Tan, J., Wang, X., Roedenbeck, C., Chevallier, F., Piao, S.L., Moriarty, R., Broquet, G.,
707 Le Quéré, C., Canadell, J.G., and Peng, S.: Five decades of northern land carbon uptake revealed
708 by the interhemispheric CO 2 gradient, Nature, 568, 221-225, https://doi.org/10.1038/s41586-019-
709 1078-6, 2019.

712 Crisp, D., Fisher, B. M., O'Dell, C., Frankenberg, C., Basilio, R., Bösch, H., Brown, L. R., Castano,
713 R., Connor, B., Deutscher, N. M., Eldering, A., Griffith, D., Gunson, M., Kuze, A., Mandrake, L.,
714 McDuffie, J., Messerschmidt, J., Miller, C. E., Morino, I., Natraj, V., Notholt, J., O'Brien, D. M.,
715 Oyafuso, F., Polonsky, I., Robinson, J., Salawitch, R., Sherlock, V., Smyth, M., Suto, H., Taylor,
716 T. E., Thompson, D. R., Wennberg, P. O., Wunch, D., and Yung, Y. L.: The ACOS CO_2 retrieval
717 algorithm – Part II: Global X_{CO2} data characterization, Atmos. Meas. Tech., 5, 687–707,
718 https://doi.org/10.5194/amt-5-687-2012, 2012.

720 Crisp, D., Pollock, H. R., Rosenberg, R., Chapsky, L., Lee, R. A. M., Oyafuso, F. A., Frankenberg,
721 C., O'Dell, C. W., Bruegge, C. J., Doran, G. B., Eldering, A., Fisher, B. M., Fu, D., Gunson, M.
722 R., Mandrake, L., Osterman, G. B., Schwandner, F. M., Sun, K., Taylor, T. E., Wennberg, P. O.,
723 and Wunch, D.: The on-orbit performance of the Orbiting Carbon Observatory-2 (OCO-2)
724 instrument and its radiometrically calibrated products, Atmos. Meas. Tech., 10, 59–81,
725 https://doi.org/10.5194/amt-10-59-2017, 2017.

727 Crowell, S., Baker, D., Schuh, A., Basu, S., Jacobson, A. R., Chevallier, F., Liu, J., Deng, F., Feng,
728 L., McKain, K., Chatterjee, A., Miller, J. B., Stephens, B. B., Eldering, A., Crisp, D., Schimel, D.,
729 Nassar, R., O'Dell, C. W., Oda, T., Sweeney, C., Palmer, P. I., and Jones, D. B. A.: The 2015–

730   2016 carbon cycle as seen from OCO-2 and the global in situ network, Atmos. Chem. Phys., 19,
731   9797–9831, https://doi.org/10.5194/acp-19-9797-2019, 2019.
732
733   Falk, M., Wharton, S., Schroeder, M., Ustin, S., and U, K.T.P.: Flux partitioning in an old-growth
734   forest: seasonal   and   interannual   dynamics. Tree   Physiol., 28,   509-520,
735   https://doi.org/10.1093/treephys/28.4.509, 2008.
736
737   Friedlingstein, P., Meinshausen, M., Arora, V.K., Jones, C.D., Anav, A., Liddicoat, S.K., and
738   Knutti, R.: Uncertainties in CMIP5 climate projections due to carbon cycle feedbacks, J. Clim., 27,
739   511-526, https://doi.org/10.1175/JCLI-D-12-00579.1, 2014.
740
741   Friedlingstein, P., Jones, M., O'Sullivan, M., Andrew, R., Hauck, J., Peters, G., Peters, W.,
742   Pongratz, J., Sitch, S., Le Quéré, C., and DBakker, O.: Global carbon budget 2019, Earth Syst. Sci.
743   Data, 11, 1783-1838, https://doi.org/10.3929/ethz-b-000385668, 2019.
744
745   Gatti, L.V., Gloor, M., Miller, J.B., Doughty, C.E., Malhi, Y., Domingues, L.G., Basso, L.S.,
746   Martinewski, A., Correia, C.S.C., Borges, V.F., and Freitas, S., 2014, Drought sensitivity of
747   Amazonian carbon balance revealed by atmospheric measurements, Nature, 506, 76-80,
748   https://doi.org/10.1038/nature12957, 2014.
749
750   Gaubert, B., Stephens, B. B., Basu, S., Chevallier, F., Deng, F., Kort, E. A., Patra, P. K., Peters,
751   W., Rödenbeck, C., Saeki, T., Schimel, D., Van der Laan-Luijkx, I., Wofsy, S., and Yin, Y.: Global
752   atmospheric CO_2 inverse models converging on neutral tropical land exchange, but disagreeing on
753   fossil fuel and atmospheric growth rate, Biogeosciences, 16, 117–134, https://doi.org/10.5194/bg-
754   16-117-2019, 2019.
755
756
757   Gurney, K.R., Law, R.M., Denning, A.S., Rayner, P.J., Pak, B.C., Baker, D., Bousquet, P.,
758   Bruhwiler, L., Chen, Y.H., Ciais, P., and Fung, I.Y.: Transcom 3 inversion intercomparison: Model
759   mean results for the estimation of seasonal carbon sources and sinks, Global Biogeochem.
760   Cycles, 18, GB1010, https://doi.org/10.1029/2003GB002111, 2004.
761
762   Henze, D. K., Hakami, A., and Seinfeld, J. H.: Development of the adjoint of GEOS-Chem, Atmos.
763   Chem. Phys., 7, 2413–2433, https://doi.org/10.5194/acp-7-2413-2007, 2007.
764
765   Jiang, Z., Worden, J. R., Worden, H., Deeter, M., Jones, D. B. A., Arellano, A. F., and Henze, D.
766   K.: A 15-year record of CO emissions constrained by MOPITT CO observations, Atmos. Chem.
767   Phys., 17, 4565–4583, https://doi.org/10.5194/acp-17-4565-2017, 2017.
768
769   Joiner, J., Guanter, L., Lindstrot, R., Voigt, M., Vasilkov, A. P., Middleton, E. M., Huemmrich, K.
770   F., Yoshida, Y., and Frankenberg, C.: Global monitoring of terrestrial chlorophyll fluorescence
771   from   moderate-spectral-resolution   near-infrared   satellite   measurements: methodology,
772   simulations,   and   application   to   GOME-2,   Atmos.   Meas.   Tech.,   6,   2803–2823,
773   https://doi.org/10.5194/amt-6-2803-2013, 2013.
774

Joiner, J., Yoshida, Y., Zhang, Y., Duveiller, G., Jung, M., Lyapustin, A., Wang, Y., & Tucker, C.: Estimation of terrestrial global gross primary production (GPP) with satellite data-driven models and eddy covariance flux data. *Remote Sensing*, **10**(9), 1346. https://doi.org/10.3390/rs10091346. 2018.

Jones, D. B. A., Bowman, K. W., Logan, J. A., Heald, C. L., Liu, J., Luo, M., Worden, J., and Drummond, J.: The zonal structure of tropical O_3 and CO as observed by the Tropospheric Emission Spectrometer in November 2004 – Part 1: Inverse modeling of CO emissions, Atmos. Chem. Phys., 9, 3547–3562, https://*doi*.org/*10.5194/acp-9-3547-2009* , 2009.

Keppel-Aleks, G., Wennberg, P. O., Washenfelder, R. A., Wunch, D., Schneider, T., Toon, G. C., Andres, R. J., Blavier, J.-F., Connor, B., Davis, K. J., Desai, A. R., Messerschmidt, J., Notholt, J., Roehl, C. M., Sherlock, V., Stephens, B. B., Vay, S. A., and Wofsy, S. C.: The imprint of surface fluxes and transport on variations in total column carbon dioxide, Biogeosciences, 9, 875–891, https://doi.org/10.5194/bg-9-875-2012, 2012.

Kiel, M., O'Dell, C. W., Fisher, B., Eldering, A., Nassar, R., MacDonald, C. G., and Wennberg, P. O.: How bias correction goes wrong: measurement of X_{CO2} affected by erroneous surface pressure estimates, Atmos. Meas. Tech., 12, 2241–2259, https://doi.org/10.5194/amt-12-2241-2019, 2019.

Konings, A. G., Bloom, A. A., Liu, J., Parazoo, N. C., Schimel, D. S., and Bowman, K. W.: Global satellite-driven estimates of heterotrophic respiration, Biogeosciences, 16, 2269–2284, https://doi.org/10.5194/bg-16-2269-2019, 2019.

Kulawik, S. S., Crowell, S., Baker, D., Liu, J., McKain, K., Sweeney, C., Biraud, S. C., Wofsy, S., O'Dell, C. W., Wennberg, P. O., Wunch, D., Roehl, C. M., Deutscher, N. M., Kiel, M., Griffith, D. W. T., Velazco, V. A., Notholt, J., Warneke, T., Petri, C., De Mazière, M., Sha, M. K., Sussmann, R., Rettinger, M., Pollard, D. F., Morino, I., Uchino, O., Hase, F., Feist, D. G., Roche, S., Strong, K., Kivi, R., Iraci, L., Shiomi, K., Dubey, M. K., Sepulveda, E., Rodriguez, O. E. G., Té, Y., Jeseck, P., Heikkinen, P., Dlugokencky, E. J., Gunson, M. R., Eldering, A., Crisp, D., Fisher, B., and Osterman, G. B.: Characterization of OCO-2 and ACOS-GOSAT biases and errors for CO_2 flux estimates, Atmos. Meas. Tech. Discuss., https://doi.org/10.5194/amt-2019-257, in review, 2019.

Kuze, A., Suto, H., Shiomi, K., Kawakami, S., Tanaka, M., Ueda, Y., Deguchi, A., Yoshida, J., Yamamoto, Y., Kataoka, F., Taylor, T. E., and Buijs, H. L.: Update on GOSAT TANSO-FTS performance, operations, and data products after more than 6 years in space, Atmos. Meas. Tech., 9, 2445–2461, https://doi.org/10.5194/amt-9-2445-2016, 2016.

Le Quéré, C., Andrew, R. M., Friedlingstein, P., Sitch, S., Pongratz, J., Manning, A. C., Korsbakken, J. I., Peters, G. P., Canadell, J. G., Jackson, R. B., Boden, T. A., Tans, P. P., Andrews, O. D., Arora, V. K., Bakker, D. C. E., Barbero, L., Becker, M., Betts, R. A., Bopp, L., Chevallier, F., Chini, L. P., Ciais, P., Cosca, C. E., Cross, J., Currie, K., Gasser, T., Harris, I., Hauck, J., Haverd, V., Houghton, R. A., Hunt, C. W., Hurtt, G., Ilyina, T., Jain, A. K., Kato, E., Kautz, M., Keeling, R. F., Klein Goldewijk, K., Körtzinger, A., Landschützer, P., Lefèvre, N., Lenton, A., Lienert, S., Lima, I., Lombardozzi, D., Metzl, N., Millero, F., Monteiro, P. M. S., Munro, D. R., Nabel, J. E.

821   M. S., Nakaoka, S., Nojiri, Y., Padin, X. A., Peregon, A., Pfeil, B., Pierrot, D., Poulter, B., Rehder,
822   G., Reimer, J., Rödenbeck, C., Schwinger, J., Séférian, R., Skjelvan, I., Stocker, B. D., Tian, H.,
823   Tilbrook, B., Tubiello, F. N., van der Laan-Luijkx, I. T., van der Werf, G. R., van Heuven, S.,
824   Viovy, N., Vuichard, N., Walker, A. P., Watson, A. J., Wiltshire, A. J., Zaehle, S., and Zhu, D.:
825   Global Carbon Budget 2017, Earth Syst. Sci. Data, 10, 405–448, https://doi.org/10.5194/essd-10-
826   405-2018, 2018.

828   Liu, J., Baskarran, L., Bowman, K., Schimel, D., Bloom, A. A., Parazoo, N., Oda, T., Carrol, D.,
829   Menemenlis, D., Joiner, J., Commane, R., Daube, B., Gatti, L. V., McKain, K., Miller, J.,
830   Stephens, B. B., Sweeney, C., & Wofsy, S. (2020). *CMS-Flux NBE 2020* [Data set]. NASA.
831   https://doi.org/10.25966/4V02-C391

833   Liu, J. and Bowman, K.: A method for independent validation of surface fluxes from atmospheric
834   inversion: Application   to   CO2, Geophys.   Res.   Lett., 43,   3502-3508,
835   https://doi.org/10.1002/2016GL067828, 2016.

837   Liu, J., Bowman, K. W., and Henze, D. K.: Source-receptor relationships of column-average
838   CO_2 and implications for the impact of observations on flux inversions. *J. Geophys. Res.*
839   *Atmos.*, 120, 5214– 5236. doi: 10.1002/2014JD022914, 2015

841   Liu, J., Bowman, K.W., Lee, M., Henze, D.K., Bousserez, N., Brix, H., James Collatz, G.,
842   Menemenlis, D., Ott, L., Pawson, S., and Jones, D.: Carbon monitoring system flux estimation and
843   attribution: impact of ACOS-GOSAT XCO2 sampling on the inference of terrestrial biospheric
844   sources   and   sinks. Tellus   B Chem.   Phys.   Meteorol.   B., 66,   22486,
845   http://dx.doi.org/10.3402/tellusb.v66.22486, 2014.

847   Liu, J., Bowman, K.W., Schimel, D.S., Parazoo, N.C., Jiang, Z., Lee, M., Bloom, A.A., Wunch,
848   D., Frankenberg, C., Sun, Y., and O'Dell, C.W.: Contrasting carbon cycle responses of the tropical
849   continents   to   the   2015–2016   El   Niño. Science, 358,   eaam5690,
850   https://doi.org/10.1126/science.aam5690, 2017.

852   Liu, J., Bowman, K., Parazoo, N.C., Bloom, A.A., Wunch, D., Jiang, Z., Gurney, K.R., and
853   Schimel, D.: Detecting drought impact on terrestrial biosphere carbon fluxes over contiguous US
854   with   satellite   observations. Environ.   Res.   Lett., 13,   095003,   https://doi.org/10.1088/1748-
855   9326/aad5ef, 2018.

858   Lovenduski, N.S. and Bonan, G.B.: Reducing uncertainty in projections of terrestrial carbon
859   uptake, Environ. Res. Lett., 12, 044020, https://doi.org/10.1088/1748-9326/aa66b8, 2017.

861   Nassar, R., Jones, D.B., Suntharalingam, P., Chen, J.M., Andres, R.J., Wecht, K.J., Yantosca, R.M.,
862   Kulawik, S.S., Bowman, K.W., Worden, J.R., and Machida, T.: Modeling global atmospheric CO2
863   with improved emission inventories and CO2 production from the oxidation of other carbon
864   species. Geosci. Model Dev., 3, 689-716, https://doi.org/10.5194/gmd-3-689-2010, 2010.
865

866 Oda, T., Maksyutov, S., and Andres, R. J.: The Open-source Data Inventory for Anthropogenic
867 CO_2, version 2016 (ODIAC2016): a global monthly fossil fuel CO_2 gridded emissions data product
868 for tracer transport simulations and surface flux inversions, Earth Syst. Sci. Data, 10, 87–107,
869 https://doi.org/10.5194/essd-10-87-2018, 2018.

871 O'Dell, C. W., Connor, B., Bösch, H., O'Brien, D., Frankenberg, C., Castano, R., Christi, M.,
872 Eldering, D., Fisher, B., Gunson, M., McDuffie, J., Miller, C. E., Natraj, V., Oyafuso, F., Polonsky,
873 I., Smyth, M., Taylor, T., Toon, G. C., Wennberg, P. O., and Wunch, D.: The ACOS CO_2 retrieval
874 algorithm – Part 1: Description and validation against synthetic observations, Atmos. Meas. Tech.,
875 5, 99–121, https://doi.org/10.5194/amt-5-99-2012, 2012.

877 O'Dell, C., Eldering, A., Wennberg, P.O., Crisp, D., Gunson, M., Fisher, B., Frankenberg, C., Kiel,
878 M., Lindqvist, H., Mandrake, L., and Merrelli, A.: Improved retrievals of carbon dioxide from
879 Orbiting Carbon Observatory-2 with the version 8 ACOS algorithm, Atmos. Meas. Tech., 11,
880 6539–6576, https://doi.org/10.5194/amt-11-6539-2018, 2018.

882 Olsen, S.C. and Randerson, J.T.: Differences between surface and column atmospheric CO2 and
883 implications for carbon cycle research, J. Geophys. Res: Atmos., 109, D02301,
884 https://doi.org/10.1029/2003JD003968, 2004.

886 Parazoo, N.C., Bowman, K., Fisher, J.B., Frankenberg, C., Jones, D.B.A., Cescatti, A., Pérez-
887 Priego, Ó., Wohlfahrt, G. and Montagnani, L.: Terrestrial gross primary production inferred from
888 satellite fluorescence and vegetation models. Glob Change Biol, 20: 3103-3121.
889 doi:10.1111/gcb.12652. 2014.

891 Poulter, B., Frank, D., Ciais, P., Myneni, R.B., Andela, N., Bi, J., Broquet, G., Canadell, J.G.,
892 Chevallier, F., Liu, Y.Y., and Running, S.W.: Contribution of semi-arid ecosystems to interannual
893 variability of the global carbon cycle, Nature, 509, 600-603, https://doi.org/10.1038/nature13376,
894 2014.

896 Quetin, G., Bloom, A. A., Bowman, K. W., & Konings, A.: Carbon flux variability from a
897 relatively simple ecosystem model with assimilated data is consistent with terrestrial biosphere
898 model estimates. *Journal of Advances in Modeling Earth Systems*, 12,
899 e2019MS001889. https://doi.org/10.1029/2019MS001889, 2020

901 Randerson, J.T., Van Der Werf, G.R., Giglio, L., Collatz, G.J., and Kasibhatla, P.S.: Global Fire
902 Emissions Database, Version 4.1 (GFEDv4), ORNL DAAC, Oak Ridge, Tennessee,
903 USA, https://doi.org/10.3334/ORNLDAAC/1293, 2018.

905 Rienecker, M.M., Suarez, M.J., Gelaro, R., Todling, R., Bacmeister, J., Liu, E., Bosilovich, M.G.,
906 Schubert, S.D., Takacs, L., Kim, G.K., and Bloom, S.: MERRA: NASA's modern-era
907 retrospective analysis for research and applications, J. Clim., 24, 3624-3648,
908 https://doi.org/10.1175/JCLI-D-11-00015.1, 2011.

910 Running, S.W., Baldocchi, D.D., Turner, D.P., Gower, S.T., Bakwin, P.S., and Hibbard, K.A.: A
911 global terrestrial monitoring network integrating tower fluxes, flask sampling, ecosystem

912 modeling and EOS satellite data, Remote Sens. Environ., 70, 108-127,
913 https://doi.org/10.1016/S0034-4257(99)00061-9, 1999.

914

915 Schuh, A.E., Jacobson, A.R., Basu, S., Weir, B., Baker, D., Bowman, K., Chevallier, F., Crowell,
916 S., Davis, K.J., Deng, F., and Denning, S.: Quantifying the impact of atmospheric transport
917 uncertainty on CO2 surface flux estimates, Global Biogeochem. Cy., 33, 484-500,
918 https://doi.org/10.1029/2018GB006086, 2019.

919

920 Sellers, P.J., Schimel, D.S., Moore, B., Liu, J., and Eldering, A.: Observing carbon cycle–climate
921 feedbacks from space, PNAS, 115, 7860-7868, https://doi.org/10.1073/pnas.1716613115, 2018.

922

923 Stephens, B.B., Gurney, K. R., Tans, P. P., *et al*.:. Weak northern and strong tropical land carbon
924 uptake from vertical profiles of atmospheric CO_2. *Science* **316**: 1732– 35,
925 doi:10.1126/science.1137004. 2007

926

927 Stephens, B., et al. 2017. ORCAS Airborne Oxygen Instrument. Version 1.0. UCAR/NCAR -
928 Earth Observing Laboratory. https://doi.org/10.5065/D6N29VC6.

929 Sweeney, C., Karion, A., Wolter, S., et al.: Seasonal climatology of CO_2 across North America
930 from aircraft measurements in the NOAA/ESRL Global Greenhouse Gas Reference Network. *J.*
931 *Geophys. Res. Atmos.*, 120, 5155– 5190. doi: 10.1002/2014JD022591. 2015

932

933 Suntharalingam, P., Jacob, D.J., Palmer, P.I., Logan, J.A., Yantosca, R.M., Xiao, Y., Evans, M.J.,
934 Streets, D.G., Vay, S.L., and Sachse, G.W.: Improved quantification of Chinese carbon fluxes
935 using CO2/CO correlations in Asian outflow, J. Geophys. Res.: Atmos., 109, D18S18,
936 https://doi.org/10.1029/2003JD004362, 2004.

937

938 Tramontana, G., Jung, M., Schwalm, C. R., Ichii, K., Camps-Valls, G., Ráduly, B., Reichstein, M.,
939 Arain, M. A., Cescatti, A., Kiely, G., Merbold, L., Serrano-Ortiz, P., Sickert, S., Wolf, S., and
940 Papale, D.: Predicting carbon dioxide and energy fluxes across global FLUXNET sites with
941 regression algorithms, Biogeosciences, 13, 4291–4313, https://doi.org/10.5194/bg-13-4291-2016,
942 2016.

943

944 van der Werf, G. R., Randerson, J. T., Giglio, L., Gobron, N., and Dolman, A. J.: Climate
945 controls on the variability of fires in the tropics and subtropics, *Global Biogeochem. Cycles*, 22,
946 GB3028, doi:10.1029/2007GB003122. 2008

947

948 Wofsy, S. C.: HIAPER Pole-to-Pole Observations (HIPPO): Fine-grained, global-scale
949 measurements of climatically important atmospheric gases and aerosols, Philos. Trans. R. Soc. A-
950 Math. Phys. Eng. Sci., 369, 2073– 2086, https://doi.org/10.1098/rsta.2010.0313, 2011.

951

952 Wofsy, S.C., Afshar, S., Allen, H.M., Apel, E., Asher, E.C., Barletta, B., Bent, J., Bian, H., Biggs,
953 B.C., Blake, D.R., and Blake, N.: ATom: Merged Atmospheric Chemistry, Trace Gases, and
954 Aerosols, ORNL DAAC, Oak Ridge, Tennessee,
955 USA, https://doi.org/10.3334/ORNLDAAC/1581, 2018.

956

957   Wunch, D., Toon, G.C., Blavier, J.F.L., Washenfelder, R.A., Notholt, J., Connor, B.J., Griffith,
958   D.W., Sherlock, V., and Wennberg, P.O.: The total carbon column observing network, Philos.
959   Trans. R. Soc. A, 369, 2087-2112, https://doi.org/10.1098/rsta.2010.0240, 2011.
960
961   Yang, Z., Washenfelder, R. A., Keppel-Aleks, G., Krakauer, N. Y., Randerson, J. T., Tans, P.
962   P., Sweeney, C., and Wennberg, P. O.: New constraints on Northern Hemisphere growing season
963   net flux, Geophys. Res. Lett., 34, L12807, https://doi.org/10.1029/2007GL029742, 2007.
964
965   Yin, Y., Bowman, K., Bloom, A.A., and Worden, J.: Detection of fossil fuel emission trends in the
966   presence   of   natural   carbon   cycle   variability, Environ.   Res.   Lett., 14,   084050,
967   https://doi.org/10.1088/1748-9326/ab2dd7, 2019.
968
969   Zhu, C., Byrd, R.H., Lu, P., and Nocedal, J.: Algorithm 778: L-BFGS-B: Fortran subroutines for
970   large-scale   bound-constrained   optimization, ACM   Trans.   Math.   Softw., 23,   550-560,
971   https://doi.org/10.1145/279232.279236, 1997.
972
973
974

975
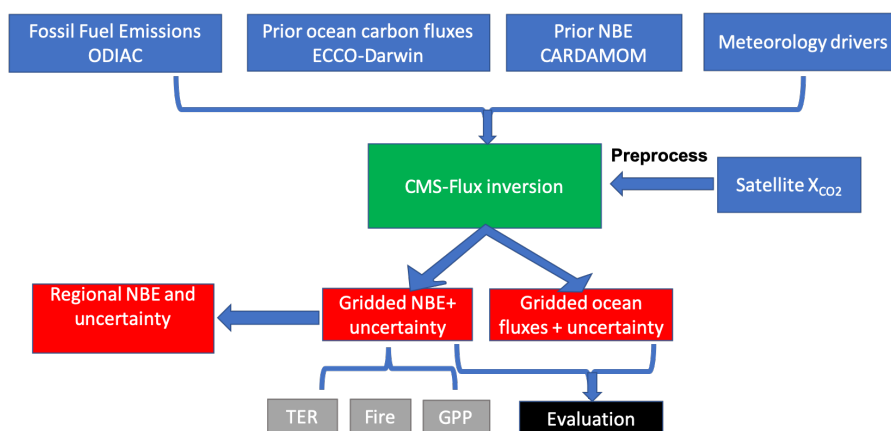
Figure: 1 Data flow diagram with the main processing steps to generate regional net biosphere change (NBE). TER: total ecosystem respiration; GPP: gross primary production. The green box is the inversion system. The blue boxes are the inputs for the inversion system. The red boxes are the data outputs from the system. The black box is the evaluation step, and the grey boxes are the future additions to the product.

981

982

983

984

985

986
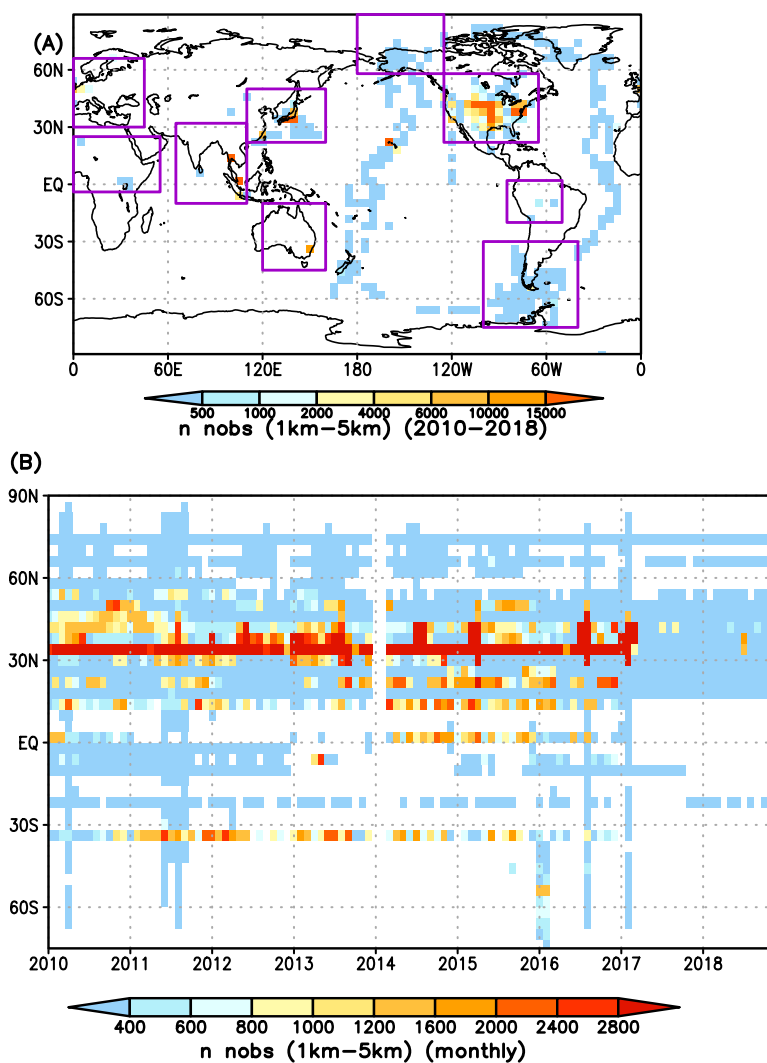
Figure: 2 The spatial and temporal distributions of aircraft observations used in evaluation of posterior NBE. (A) The total number of aircraft observations between 1–5 km between 2010–2018 at each 4° x 5°grid point. The rectangle boxes show the range of the nine sub regions. (B) The total number of monthly aircraft observations at each longitude as a function of time.

992

993

994
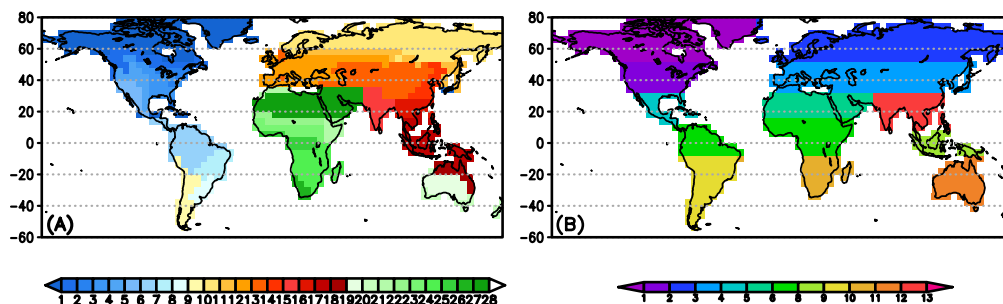
Figure: 3 Two types of regional masks used in calculating regional fluxes. The mask in (A) is based on a combination of condensed seven MODIS IGBP plant functional types, TRANCOM-3 regions (Gurney et al., 2004), and continents. The mask in (B) is based on latitude and continents.

999

1000

1001

1002

1003

1004

1005

1006
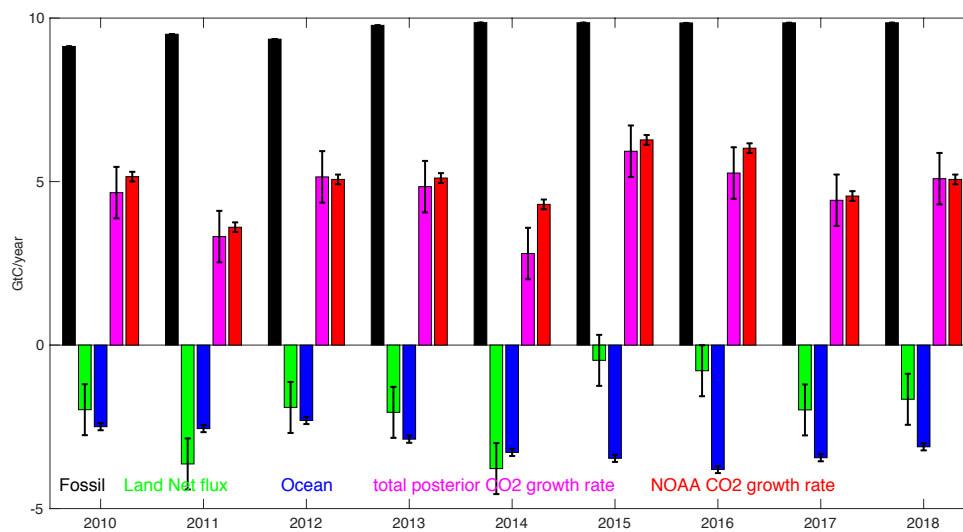
1007

Figure: 4 Global flux estimation and uncertainties from 2010 −2018 (black: fossil fuel; green: posterior land fluxes; blue: ocean fluxes; magenta: estimated CO_2 growth rate; red: NOAA CO_2 growth rate).

1008
1009
1010
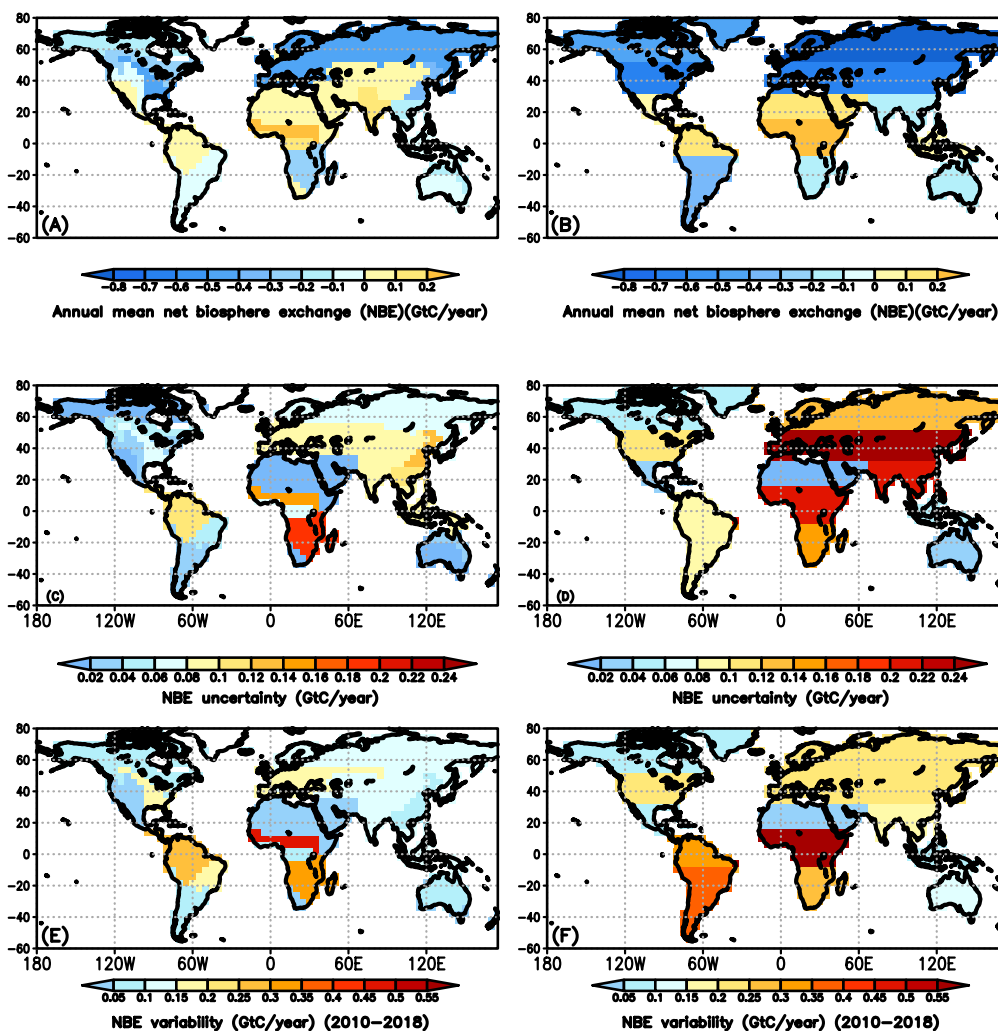
1011
1012 **Figure: 5 Mean annual regional NBE (A and B), uncertainty (C and D), and variability**
1013 **between 2010–2018 (E and F) with two types of regional masks.**
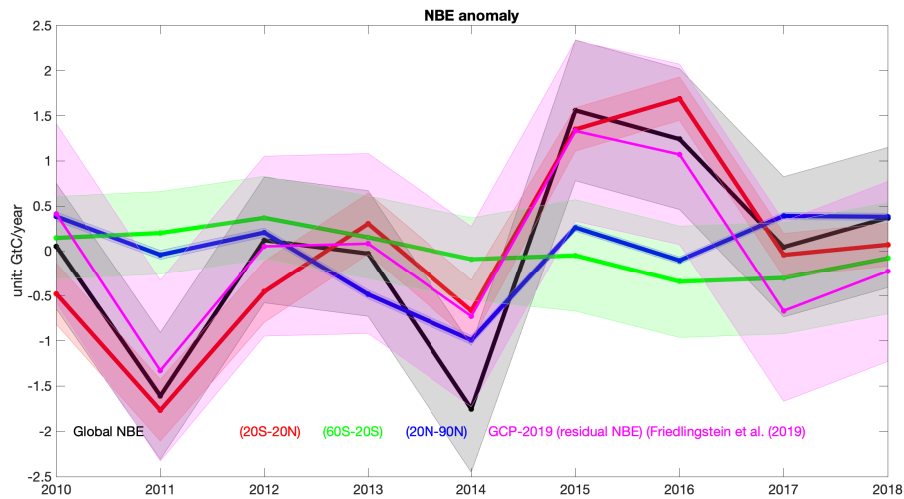
1014

Figure: 6 The NBE interannual variability over the globe (black), the tropics (20°S–20°N), SH mid-latitudes (60°S–20°S), and NH mid-latitudes (20°N–9°0N). For reference, the residual net land carbon sink from GCP (Friedlingstein et al., 2019) and its uncertainty is also shown (magenta).

1015
1016
1017
1018
1019
1020
1021
1022

1023

Figure: 7 The NBE interannual variability over six selected regions. Blue: annual NBE anomaly and its uncertainties. Green: annual GPP anomaly based on FLUXSAT.
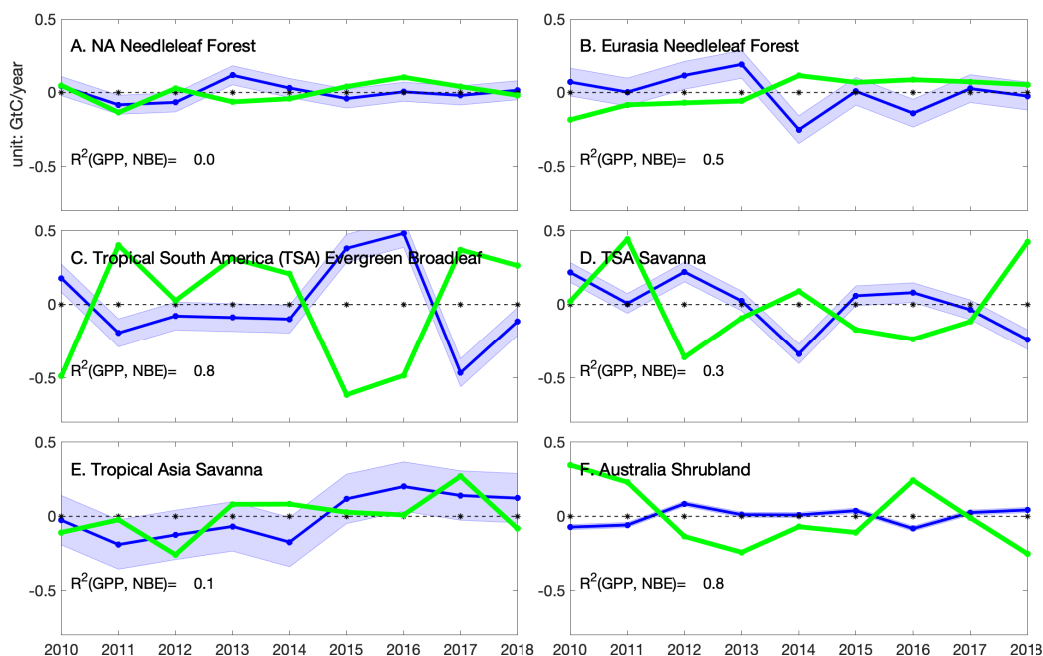
1024
1025
1026
1027
1028
1029
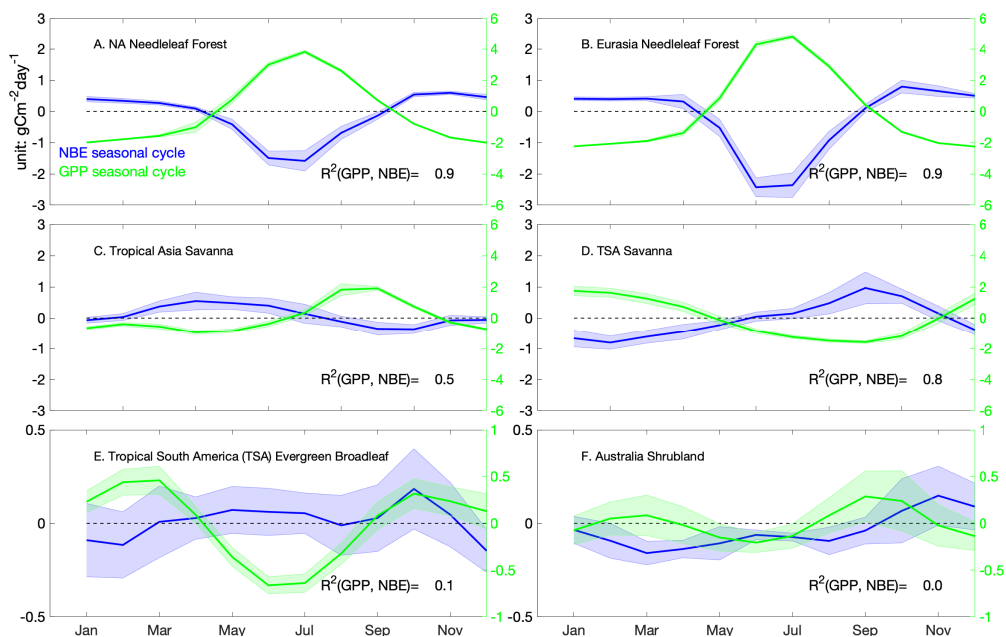
1030

Figure: 8 Blue: climatological NBE seasonality over six selected regions shown in Figure 3A; blue shaded: NBE monthly uncertainty and variability (1-sigma) over nine years. Green and shaded: monthly mean GPP and its variability (1-sigma) over nine years. The names of each region are shown on individual subplots.

1031
1032
1033
1034
1035

1036

1037
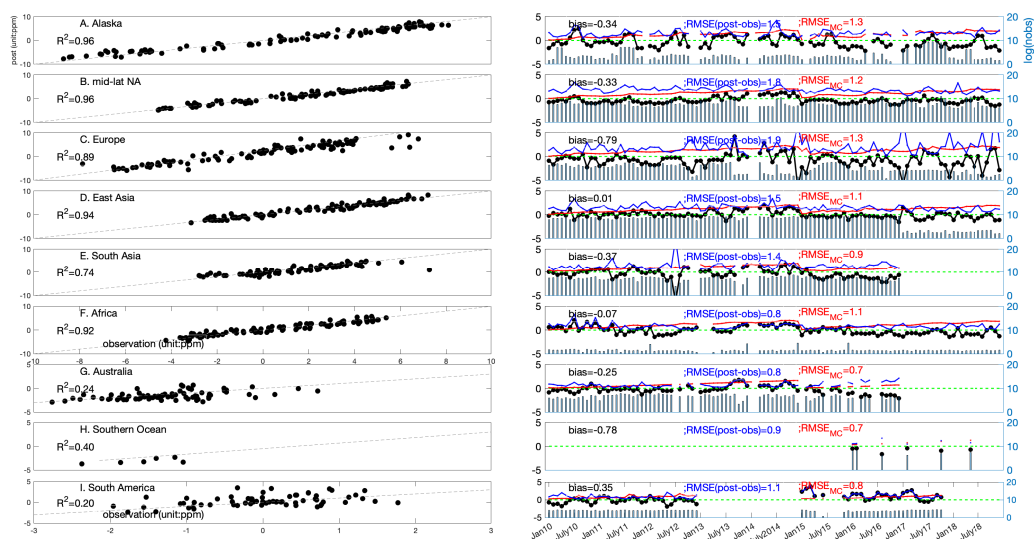
1038

Figure: 9 Comparison between posterior CO_2 mole fraction and aircraft observations. Left panel: detrended posterior CO_2 (y-axis) vs. detrended aircraft CO_2 (x-axis) over nine regions. The dashed line is 1:1 line; right panel: black: the differences between posterior CO_2 and aircraft CO_2 as a function of time; blue: RMSE (unit: ppm); red: $RMSE_{MC}$. The blue bar shows the number of aircraft observations (log scale) as a function of month.

1039
1040
1041
1042
1043
1044

1045
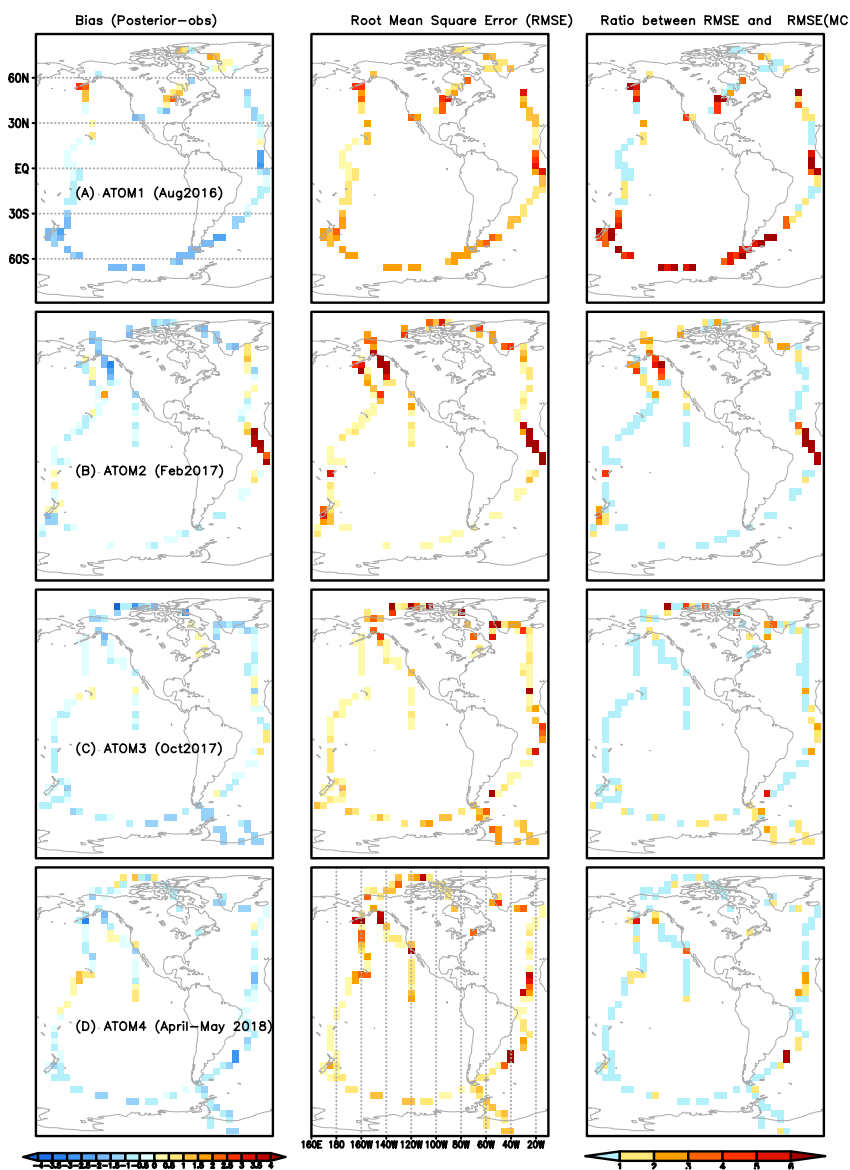
1046

Figure: 10 Left column: the mean differences between posterior CO$_2$ and aircraft observations from ATOM 1–4 aircraft campaigns between 1–5 km (A–D). Middle column: the Root Mean Square Errors (RMSE) between aircraft observations and posterior CO$_2$ between 1–5 km. The color bar is the same as the left column. Right column: the ratio between RMSE and RMES$_{MC}$ based on ensemble CO$_2$ from the Monte Carlo uncertainty estimation method.
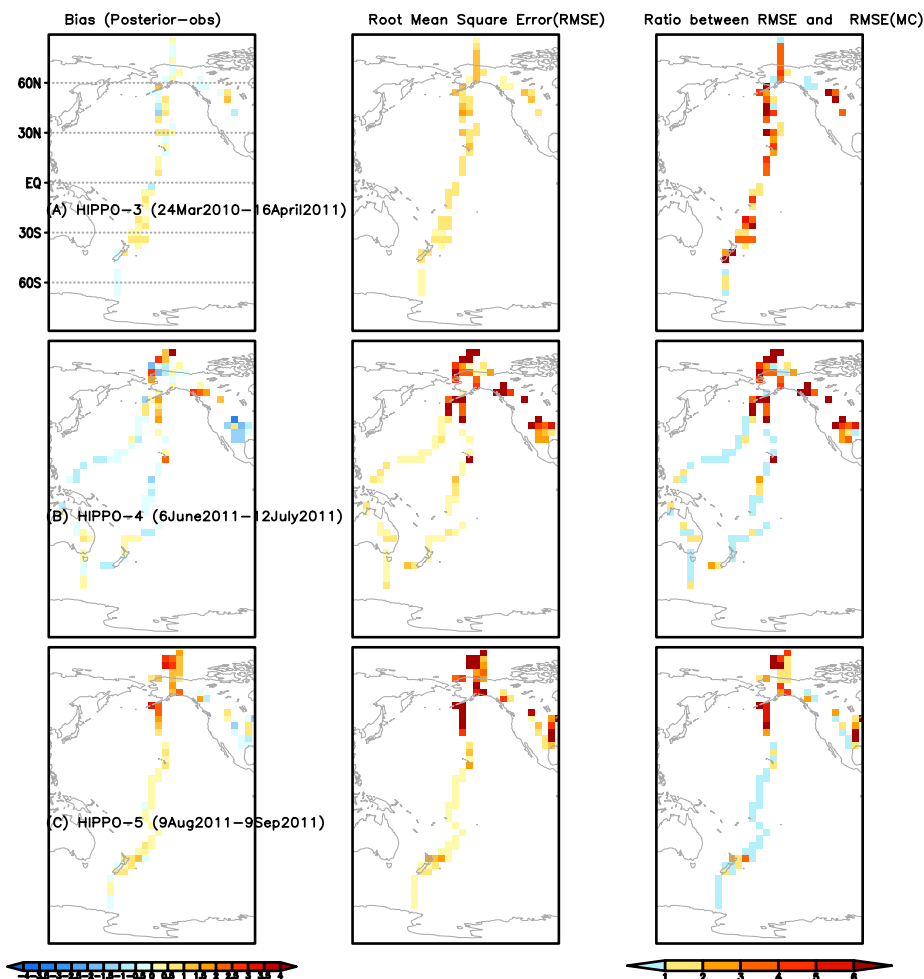
1053

Figure: 11 Left column: the mean differences between posterior CO$_2$ and aircraft observations from HIPPO 3-5 aircraft campaigns between 1–5 km (A–C) (unit: ppm). (unit: ppm). The time frame of each campaign is in the figure. Middle column: the Root Mean Square Errors (RMSE) between aircraft observations and posterior CO$_2$ between 1–5 km (unit: ppm). The color bar is the same as the left column. Right column: the ratio between RMSE and RMSE$_{MC}$ based on ensemble CO$_2$ from the Monte Carlo method.

1060
1061
1062
1063
1064
1065
1066

1067

1068 **Table: 1 Configurations of the CMS-Flux atmospheric inversion system**

	Model setup	**Configuration**	**Reference**
Inversion general setup	Spatial scale	Global	--
	Spatial resolution	4° latitude x 5° longitude	
	Time resolution	monthly	
	Minimizer of cost function	L-BFGS	Byrd et al., 1994; Zhu et al., 1997
	Control vector	Monthly net terrestrial biosphere fluxes and ocean fluxes	
Transport model	Model name	GEOS-Chem and its adjoint	Suntharalingam et al., 2004 Nassar et al., 2010 Henze et al., 2007
	Meteorological forcing	GEOS-5 (2010–2014) and GEOS-FP (2015–2019)	Rienecker et al., 2008

1069

1070

1071

1072 **Table: 2 Description of the prior fluxes and assumed uncertainties in the inversion system**

Prior fluxes	Terrestrial biosphere fluxes	Ocean fluxes	Fossil fuel emissions
Model name	CARDAMOM-v1	ECCO-Darwin	ODIAC 2018
Spatial resolution	4° x 5°	0.5°	1° x 1°
Frequency	3-hourly	3-hourly	hourly
Uncertainty	Estimated from CARDAMOM	100% same as Liu et al. (2017)	No uncertainty
References	Bloom et al., 2006; 2020	Brix et al, 2015; Carroll et al., 2020	Oda et al., 2016; 2018

1073

1074

1075

1076

1077 **Table: 3 Description of observation and evaluation dataset. Data sources are listed in Table 7.**

	Dataset name and version	References
Satellite X_{CO_2}	ACOS-GOSAT v7.3	O'Dell et al., (2012)
	OCO-2 v9	O'Dell et al., (2018)
Aircraft CO_2 observations	ObsPack OCO-2 MIP	CarbonTracker team (2019)
	HIPPO 3-5	Wofsy et al. (2011)
	ATOM 1-4	Wofsy et al.(2018)
	INPE	Gatti et al., (2014)
	ORCAS	Stephens et al., 2017
GPP	FLUXSAT-GPP	Joiner et al., (2018)

1078

1079

1080

1081 **Table: 4 Latitude and longitude ranges for seven sub regions.**

Region	Alaska	Mid-lat NA	Europe	East Asia	South Asia
Longitude range	180°W–125° W	125°W–65°W	5°W–45°E	110°E–160°E	65°E–110°E
Latitude range	58°N–89°N	22°N-58°N	30°N–66°N	22°N–50°N	10°S–32°N
Region	Africa	South America	Australia	Southern Ocean	
Longitude range	5°W–55°E	95°W–50°W	120°E–160°E	110°W–40°E	
Latitude range	2°N–18°N	20°S–2°N	45°S–10°S	80°S–30°S	

1082

1083

1084

1085   **Table: 5 List of the data products.**

Product	Spatial resolution	Temporal resolution when applicable	Data format	Sample data description in the text
Total fossil fuel, ocean, and land fluxes	Global	Annual	*csv*	Figure 4 (section 4.1)
Climatology mean NBE, variability, and uncertainties	PFT and continents based 28 regions	N/A	*csv*	Figure 5 (section 4.2)
	Geographic-based 13 regions		*csv*	
Hemispheric NBE and uncertainties	NH (20°N-90°N), tropics (20°S-20°N), and SH (60°S-20°S)	Annual	*csv*	Figure 6 (section 4.3)
NBE variability and uncertainties	PFT and continents based 28 regions	Annual	*csv*	Figure 7 (section 4.3)
	Geographic -based 13 regions		*csv*	
NBE seasonality and its uncertainties	PFT and continents based 28 regions	Monthly	*csv*	Figure 8 (section 4.4)
	Geographic -based 13 regions		*csv*	
Monthly NBE and uncertainties	PFT and continents based 28 regions	Monthly	*csv*	N/A
	Geographic -based 13 regions		*csv*	
Gridded NBE and uncertainties	4° (latitude) x 5° (longitude)	Monthly	*NetCDF*	N/A
Region masks	PFT and continents based 28 regions	N/A	csv	Figure 3 (section 2.4)
	Geographic -based 13 regions		csv	
Fluxes at a few selected flux tower sites		Monthly	*csv*	N/A

1086

1087

1088

1089

1090 **Table: 6 The nine-year mean regional annual fluxes, uncertainties, and variability. Regions**
1091 **are based on the mask shown in Figure 5A (Figure 5.csv). Unit: GtC/year**

Region name (Figure4.csv)	Mean NBE	Uncertainty	Variability
NA shrubland	-0.14	0.02	0.05
NA needleleaf forest	-0.22	0.04	0.06
NA deciduous forest	-0.2	0.04	0.07
NA crop natural vegetation	-0.41	0.06	0.18
NA grassland	-0.04	0.03	0.03
NA savannah	0.03	0.02	0.03
Tropical South America (SA) evergreen broadleaf	0.04	0.1	0.28
SA savannah	-0.09	0.06	0.18
SA cropland	-0.07	0.03	0.07
SA shrubland	-0.03	0.02	0.08
Eurasia shrubland savanna	-0.44	0.07	0.14
Eurasia needleleaf forest	-0.41	0.07	0.12
Europe cropland	-0.46	0.09	0.16
Eurasia grassland	0.02	0.08	0.13
Asia cropland	-0.37	0.13	0.08
India	0.14	0.09	0.14
Tropical Asia savanna	-0.12	0.11	0.08
Tropical Asia evergreen broadleaf	-0.09	0.09	0.12
Australia (Aus) savannah grassland	-0.11	0.02	0.09
Aus shrubland	-0.07	0.01	0.05
Aus cropland	-0.01	0.01	0.03
African (Afr) northern shrubland	0.04	0.02	0.03
Afr grassland	0.03	0.01	0.01
Afr northern savanna	0.54	0.15	0.49
Afr southern savanna	-0.27	0.18	0.33
Afr evergreen broadleaf	0.1	0.07	0.09
Afr southern shrubland	0.01	0.01	0.01
Afr desert	0.06	0.01	0.04

1092

1093

1094

1095 **Table: 7 Lists of data sources used in producing and evaluating posterior NBE product.**

Data name	Data Source
ECCO-Darwin ocean fluxes	https://data.nas.nasa.gov/ecco
CARDAMOM NBE and uncertainties	https://doi.org/10.25966/4v02-c391
ODIAC	http://db.cger.nies.go.jp/dataset/ODIAC/DL_odiac2019.html
GOSAT b7.3	https://oco2.gesdisc.eosdis.nasa.gov/data/GOSAT_TANSO_Level2/ACOS_L2S.7.3/
OCO-2 b9	https://disc.gsfc.nasa.gov/datasets?page=1&keywords=OCO-2
ObsPack	https://www.esrl.noaa.gov/gmd/ccgg/obspack/data.php
ATom 1-4	https://daac.ornl.gov/ATOM/guides/ATom_merge.html
HIPPO 3-5	https://www.eol.ucar.edu/field_projects/hippo
INPE	https://www.esrl.noaa.gov/gmd/ccgg/obspack/data.php?id=obspack_co2_1_INPE_RESTRICTED_v2.0_2018-11-13 and
FLUXSAT-GPP	https://gs614-avdc1-pz.gsfc.nasa.gov/pub/tmp/FluxSat_GPP/
Posterior NBE	https://doi.org/10.25966/4v02-c391

1096

1097
1098